AD-A081 230   WASHINGTON UNIV SEATTLE   F/G 6/18
ULTRASHORT LASER PULSE INDUCED ELECTROMAGNETIC STRESS ON BIOLOG--ETC(U)
NOV 79 A P BRUCKNER, J M SCHURR, E CHANG   F33615-76-C-0604
UNCLASSIFIED 20-2094   SAM-TR-79-3   NL

| OF |
AD
A081230

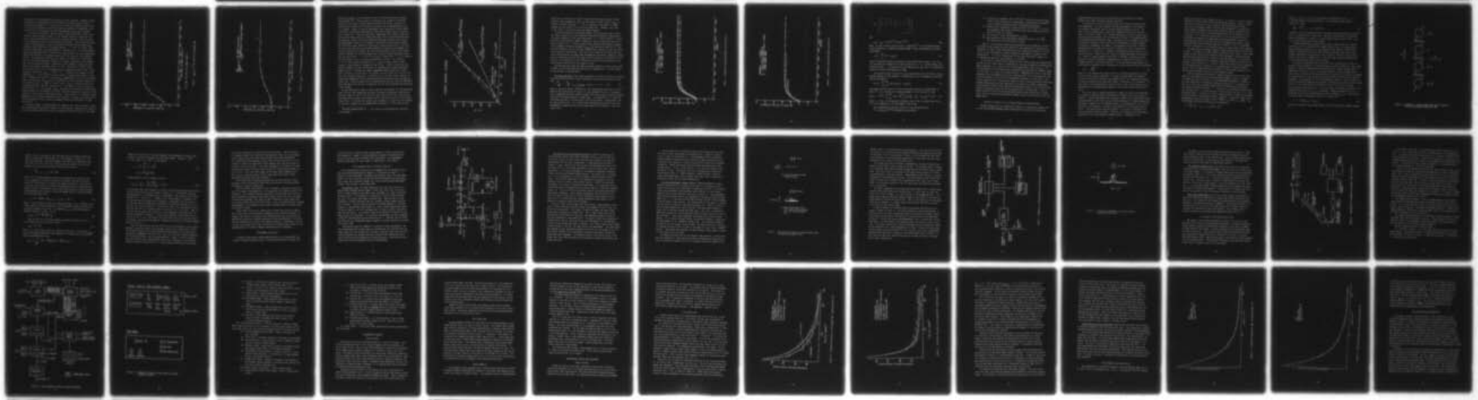

END
DATE
FILMED
3-80
DDC

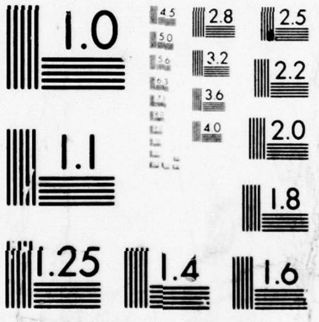

MICROCOPY RESOLUTION TEST CHART
NATIONAL BUREAU OF STANDARDS-1963-A

Report SAM-TR-79-3

2

SC

ULTRASHORT LASER PULSE INDUCED ELECTROMAGNETIC STRESS ON BIOLOGICAL MACROMOLECULAR SYSTEMS

Adam P. Bruckner, Ph.D.
J. Michael Schurr, Ph.D.
Eddie Chang, Ph.D.
Aerospace and Energetics Research Program
University of Washington
Seattle, Washington 98195

November 1979

Final Report for Period September 1976 - February 1978

Approved for public release; distribution unlimited.

Prepared for
USAF SCHOOL OF AEROSPACE MEDICINE
Aerospace Medical Division (AFSC)
Brooks Air Force Base, Texas 78235

NOTICES

This final report was submitted by the University of Washington, Seattle, Washington 98195, under contract F33615-76-C-0604, job order 7757-02-55, with the USAF School of Aerospace Medicine, Aerospace Medical Division, AFSC, Brooks Air Force Base, Texas. Dr. John Taboada (RZL) was the Laboratory Project Scientist-in-Charge.

When U.S. Government drawings, specifications, or other data are used for any purpose other than a definitely related Government procurement operation, the Government thereby incurs no responsibility nor any obligation whatsoever; and the fact that the Government may have formulated, furnished, or in any way supplied the said drawings, specifications, or other data is not to be regarded by implication or otherwise, as in any manner licensing the holder or any other person or corporation, or conveying any rights or permission to manufacture, use, or sell any patented invention that may in any way be related thereto.

This report has been reviewed by the Office of Public Affairs (PA) and is releasable to the National Technical Information Service (NTIS). At NTIS, it will be available to the general public, including foreign nations.

This technical report has been reviewed and is approved for publication.

John Taboada
JOHN TABOADA, Ph.D.
Project Scientist

Ralph G. Allen
RALPH G. ALLEN, Ph.D.
Supervisor

Lawrence J. Enders
LAWRENCE J. ENDERS
Colonel, USAF, MC
Commander

UNCLASSIFIED

SECURITY CLASSIFICATION OF THIS PAGE (*When Data Entered*)

(19) **REPORT DOCUMENTATION PAGE**		READ INSTRUCTIONS BEFORE COMPLETING FORM
1. REPORT NUMBER (18) SAM-TR-79-3	2. GOVT ACCESSION NO.	3. RECIPIENT'S CATALOG NUMBER
4. TITLE (*and Subtitle*) (6) ULTRASHORT LASER PULSE INDUCED ELECTROMAGNETIC STRESS ON BIOLOGICAL MACROMOLECULAR SYSTEMS.		5. TYPE OF REPORT & PERIOD COVERED (9) Final Report, Sep [redacted] 76 — Feb [redacted] 78,
		6. PERFORMING ORG. REPORT NUMBER (14) 20-2094
7. AUTHOR(s) (10) Adam P. Bruckner, Ph.D. J. Michael Schurr, Ph.D. Eddie Chang, Ph.D.		8. CONTRACT OR GRANT NUMBER(s) (15) F33615-76-C-0604
9. PERFORMING ORGANIZATION NAME AND ADDRESS Aerospace and Energetics Research Program University of Washington Seattle, Washington 98195 370 200		10. PROGRAM ELEMENT, PROJECT, TASK AREA & WORK UNIT NUMBERS 62202F (17) 02 (16) 7757-02-55
11. CONTROLLING OFFICE NAME AND ADDRESS USAF School of Aerospace Medicine (RZL) Aerospace Medical Division (AFSC) Brooks Air Force Base, Texas 78235		12. REPORT DATE (11) Nov [redacted] 79
		13. NUMBER OF PAGES 55
14. MONITORING AGENCY NAME & ADDRESS(*if different from Controlling Office*) (12) 59		15. SECURITY CLASS. (*of this report*) Unclassified
		15a. DECLASSIFICATION/DOWNGRADING SCHEDULE

16. DISTRIBUTION STATEMENT (*of this Report*)

Approved for public release; distribution unlimited.

17. DISTRIBUTION STATEMENT (*of the abstract entered in Block 20, if different from Report*)

18. SUPPLEMENTARY NOTES

19. KEY WORDS (*Continue on reverse side if necessary and identify by block number*)

Picosecond biological damage
Picosecond pulses
Biological macromolecules
Dynamic light scattering
Electromagnetic stress

20. ABSTRACT (*Continue on reverse side if necessary and identify by block number*)

The threshold damage mechanisms resulting from picosecond laser irradiation of biological macromolecular systems similar to constituents of living cells are examined theoretically and experimentally. Three classes of potential damage mechanisms are possible: (1) laser-induced infrared photochemistry, (2) thermal and catalytic mechanisms, and (3) stress-induced mechanical strains. A preliminary theoretical treatment is presented of the problem of stress distribution in a rodlike array of optically anisotropic elements in a viscous fluid that is exposed to an intense

→ next page

DD FORM 1 JAN 73 1473 EDITION OF 1 NOV 65 IS OBSOLETE

UNCLASSIFIED -370200 slt

SECURITY CLASSIFICATION OF THIS PAGE (*When Data Entered*)

20. ABSTRACT (cont'd)

polarized light field. The results of experimental studies with poly(L-lysine) and calf-thymus DNA are presented. Solutions of these biological macromolecules are exposed to ultrashort pulses produced by a mode-locked Nd:Glass laser at a wavelength of 1060 nm. The effects of single pulses and one or more entire pulse trains are investigated. Molecular damage is monitored by measuring changes in the molecular translational diffusion coefficients between irradiated and control samples through the technique of dynamic light scattering . Although, thus far, damage thresholds for single picosecond pulses have not been established, it has been found that energy densities of the order of 100-150 mJ/cm^2 for an entire mode-locked pulse train appear to be required to produce detectable damage in samples of DNA. Under similar conditions no damage is observed in poly(L-lysine). This suggests that in living tissue the hereditary material may be more susceptible to damage than the proteins.

cm. sq.

TABLE OF CONTENTS

LIST OF ILLUSTRATIONS

ULTRASHORT LASER PULSE INDUCED ELECTROMAGNETIC STRESS ON BIOLOGICAL MACROMOLECULAR SYSTEMS

INTRODUCTION

The ocular hazard from laser radiation has been the object of extensive study for a number of years (1-5). The effect of ultrashort (10^{-11} - 10^{-12} sec) laser pulses on retinal tissue, however, has only recently begun to receive attention. Based on the results of a recent study by Taboada at USAFSAM (5), carried out in the picosecond time regime, the damage threshold and injury mechanisms associated with picosecond pulse trains at a 1060-nm wavelength appear to differ drastically from those associated with pulses longer than about a nanosecond.

For pulse durations down to 10^{-9} sec, the injury to the tissue is believed to be caused by local temperature rise and resulting protein denaturation and enzyme inactivation. Typical threshold values of radiant exposure at the retina that cause observable lesions approach ~ 1 J/cm^2 as the exposure time is reduced to 10^{-9} sec. A recent study (4) using single 25-35-psec pulses generated by a Nd:YAG laser, found a damage threshold of similar magnitude: ~ 2 J/cm^2. Taboada (5), however, has found that for pulse durations under 10 psec, the damage threshold for pulse trains of 10-20 pulses drops drastically by about three orders of magnitude, to $\sim .002$ J/cm^2. This result suggests a different damage mechanism, one that is a function of the instantaneous electromagnetic field rather than of the total energy deposition. This is of immediate concern to the problem of establishing mode-locked laser safety standards for Air Force personnel.

The problem of laser-induced damage in optical dielectrics has been widely studied since the inception of high-power lasers (6,7). Ultrashort-pulse damage processes in such materials have been found to scale with an electron avalanche process; i.e., electric-field magnitudes in pulses that cause damage appear equivalent to those in d.c. breakdown experiments (8,9). Comparatively little work has been done on the phenomena associated with the interaction of intense ultrashort light pulses with biological media (5,10). A number of possible damage mechanisms have been suggested, such as intense acoustic transients, direct breakdown in the bulk, multiphoton ionization, and free radical formation (10). It has been suggested that the electromagnetic field in the ultrashort pulse interacts directly with the cellular membranes and drastically modifies their permeability (5). This interaction may result in direct dissociation of protein molecules or in their breakage due to induced torques. Optical field strengths of the order of 10^7 V/m appear to be sufficient for such effects.

The primary difficulties in assessing damage mechanisms in biological tissue are that, unlike the optically pure samples used in inanimate-materials studies, biological materials are heavily concentrated with optical inclusions, free-charge regions, and dielectric absorption discontinuities. Furthermore, the end point resulting from energy deposition may be reached by a complicated set of pathological changes, with a result difficult to interpret. Important constituents of living cells that are likely candidates for sites of radiation damage are: (a) its proteins, including fibrous structural and contractile proteins, enzymes, and other polypeptides; (b) its nucleic acids, which are generally found in cells to be complexed with basic proteins (histones) in a form called chromatin, or complexed with polyamines; and (c) its cell and vesicle lipid membranes.

An effort to identify the damage mechanisms in the picosecond time regime has been underway at the Unversity of Washington since September 1976. To make tractable the problem of high-transient-field stress effects on retinal tissue, this work has to date been confined to the examination of isolated biological macromolecular systems that are similar to the constituents of living cells. Accordingly, laser irradiation studies of macromolecular structures, such as calf-thymus DNA and the synthetic polypeptide poly(L-lysine), in aqueous solution have been undertaken. Solutions of these molecules have been exposed to ultrashort laser pulses produced by a mode-locked Nd:Glass laser system operating at a 1060-nm wavelength. The study has encompassed a wide range of pulse energies for both single pulses and entire trains of pulses. The goal has been to determine the pulse parameters required to break 50% of the irradiated molecules. Particle damage has been monitored principally by the technique of dynamic light scattering (11-14). This has consisted of the correlation analysis of the fluctuating intensity of He:Ne continuous-wave (CW) laser light scattered from dilute solutions of the macromolecules to measure changes in the translational diffusion coefficients between irradiated and control samples.

These studies have shown that under certain circumstances DNA macromolecules are changed, as revealed in the photon correlation spectrum, when exposed to mode-locked pulse trains of 1060-nm light. Energy densities of at least 100-500 mJ/cm^2 are required to produce detectable changes in samples of DNA, for example. Under similar conditions no damage has been observed in poly(L-lysine), which suggests that the hereditary material (i.e., DNA) is a more likely site of biological damage than the proteins. Preliminary work using frequency doubled light (530 nm) has indicated that detectable changes in DNA may be induced at this wavelength at energy levels as low as ~1 mJ/cm^2 per entire pulse train.

In addition to the experimental studies, preliminary theoretical work has been done on the problem of stress distribution in a rodlike array of optically anisotropic elements in a viscous fluid that is exposed to an intense polarized light field. It has been determined that the stress is distributed essentially uniformly along the rod when the number of elements in the array is large compared to 1.0. Thus, a random distribution of breakage products is predicted for single pulses, should this optically induced rotational stress be the predominant damage mechanism. The manner in which the average breakage-product size scales with intensity of the pulse has also been obtained for this model. The absence of breakage in the macromolecules at most of the power levels tested has so far precluded the conclusive determination of a breakage mechanism.

THEORETICAL CONSIDERATIONS

Theoretical Background of Dynamic Light Scattering Measurements

Derivation of the Dynamic Structure Factor--The dynamic information contained in the scattered light from a solution of macromolecules is used as a nonperturbative method to monitor laser-induced damage after exposure of the sample to picosecond pulses. This section will briefly review the salient aspects of dynamic light scattering, and the next section will focus on the relationship of dynamic light scattering to macromolecules, specifically DNA.

The far-field form of the scattered radiation from an induced oscillating dipole is well known. One may obtain an expression relevant to coherent dynamic scattering under the following assumptions:

(1) The Coherence Assumption. The bandwidth of the incident light must be small enough for the light field to be in phase as it travels through the scattering volume.

(2) The Quasi-Elastic Assumption. The frequency shifts in the scattered light must be small enough for the scattered field not to dephase in the scattering cell.

(3) The Coherence Volume Assumption. The dimensions of the scattering volume must be small with respect to R, the distance from the volume to the detector.

When these conditions are fulfilled, the scattered field may be written as (15)

$$E_s(R,t) = \frac{-\omega_o^{\,2}\, E_o}{C_o^{\,2}\, \varepsilon\, R}\, \alpha \exp i(K_s R - \omega t) \sum_j \exp i(\underset{\sim}{K} \cdot \underset{\sim}{r}_j(t))$$

where s refers to the scattered field, ε the dielectric constant, α the effective polarizability, and K_s the scattered wavevector; j indexes the scatterers in the scattering volume, and $\underset{\sim}{K}$ is the scattering wavevector,

$$\underset{\sim}{K} = \underset{\sim}{K}_s - \underset{\sim}{K}_o$$

whose magnitude is $\frac{4\pi}{\lambda}$ n sin (θ/2), with n the refractive index and θ the scattering angle.

The coherently scattered field at an angle θ thus arises from a single Fourier component whose wavelength is $\Lambda \equiv 2\pi/K$. $\underset{\sim}{K}$ can then be looked upon as a Bragg condition for first-order scattering.

The correlation function for $E_s(R,t)$ is

$$\langle E_s^{*}(R,0)E_s(R,t)\rangle = \left(\frac{\omega_o}{C_o}\right)^4 \left(\frac{E_o}{R\varepsilon}\right)^2 \exp[-i\,\omega_o t]\,\alpha^2 \left\langle \sum_{\ell,m} \exp[-i\,\underset{\sim}{K}\cdot\underset{\sim}{r}_\ell(o) + i\underset{\sim}{K}\cdot\underset{\sim}{r}_m(t)]\right\rangle$$

The term in brackets on the right-hand side is known as the dynamic structure factor, S(k,t), and contains the information of interest. For example, for independent, structureless Brownian particles

$$S(k,t) = e^{-DK^2t}$$

where D is the diffusion constant of the particle. Discussion of more complicated systems will be given in the next section.

Since intensity measurements by a square-law detector (PMT) are used in a dynamic light scattering experiment, one actually measures a fourth-order correlation function, $\langle E_s{}^*(R,0)E_s(R,0)E_s{}^*(R,t)E_s(R,t)\rangle$ whose structure factor is proportional to

$$N^2(1 + e^{-2DK^2t})$$

The above result is, again, strictly true for independent particles.

Analysis of Damaged Macromolecules--Determination of the size, shape, molecular weight, and degree of polydispersity of both native and damaged macromolecules in solution is the very core of the damage-assessment problem. These same quantities are the primary objectives of all traditional methods of physical biochemistry, which include ultracentrifugation, diffusion, viscosity, osmotic pressure, and classical light scattering. The comparatively recent technique of coherent dynamic light scattering (15) is nonperturbative, offers a considerable advantage in speed of measurement, and provides unique insight into the sample quality, especially regarding formation of aggregates and other high-molecular-weight species. In addition, only the latter technique offers the possibility of monitoring changes in the internal dynamics of macromolecules, which may reflect milder forms of radiation damage than outright breakage, as will be discussed further below.

In its simplest and most straightforward application, coherent dynamic light scattering provides autocorrelation functions that are single-exponential decays, the time constants of which yield the so-called Z-average diffusion coefficient (15).

$$D_z \equiv \sum_i C_iM_i^2D_i/\sum_i C_iM_i$$

where C_i and M_i are the concentration and molecular weight, respectively, of subpopulations in the sample. This technique also allows confirmation of the fact that the Brownian motion indeed obeys the free-particle diffusion equation.

Attempts to measure polydispersity in very well controlled synthetic mixtures indicate that polydispersity will be very difficult, if not impossible, to measure quantitatively in real samples (15). Among the other "physical" techniques, only ultracentrifugation allows an estimate of polydispersity--and that is offset by some considerable disadvantages, including the inability to observe internal dynamics or very large aggregates, as well as the enormously higher apparatus cost.

Unfortunately, a precise characterization of the damage will probably require measurement of the full distribution of the sizes of surviving pieces in both radiated and control samples. Toward that difficult end we have researched the options and have planned, purchased, and constructed high-resolution gel electrophoresis equipment, which is described elsewhere in this report (Conclusions and Recommendations). The disadvantage of gel electrophoresis is that it is an empirical technique that can be quantitatively applied only to homologous series of linear biopolymers of the same kind, and may not work at all for membrane vesicles and other biologically important weak association aggregates, or even whole cells, that can still be studied by dynamic light scattering techniques. Moreover, it offers no information regarding internal structure and dynamics.

For the flexible biopolymers studied in this first phase, the center-of-mass translational diffusion coefficients monitor the molecular weight according to

$D \propto M^{-0.6}$ for poly(L-lysine)

$D \propto M^{-0.45}$ for DNA

the exact exponents and coefficients depending on conditions in solution. In addition the intensity autocorrelation functions themselves, which do contain some polydispersity information, provide an extra means of comparison between samples, even those possessing the same average-diffusion coefficient. In particular, it is the essential similarity of the correlation functions at all scattering angles, for both radiated and control samples, that was the primary criterion for the negative results cited below. The Nicolet signal averager we have used is capable of storing as many as four correlation functions, and provides for both additive and multiplicative manipulation and simultaneous display of as many as four such curves, so that a detailed point-by-point comparison of the autocorrelation functions can be achieved. Although proving a quantitative interpretation of the observed similarity between curves is difficult, the suggestion is certainly very strong that there has been at most an insignificant change in either the molecular weight or distribution of molecular sizes in the samples for which the negative results were reported.

A principal advantage of coherent dynamic light scattering is that it may provide a means to detect changes in the internal dynamics of DNA that arise from single-strand breaks or from locally denatured regions, neither of which kind of damage could be easily detected by other means. This possibility stems in part from experiments in which correlation functions for polarized light scattered from solutions of calf-thymus DNA ($M_r = 11 \times 10^6$) in 1 M NaCl, both with and without EDTA, were determined as a function of pH. The latter measurements were completed prior to initiation of the contract, but the corresponding samples with EDTA were investigated during the first quarter of the contract period. The correlation functions were found in all cases to be surprisingly well fit by single exponential decays at all angles, especially at the extreme high and low scattering angles, regardless of the presence or absence of EDTA. Plots of reciprocal relaxation time vs. K^2 ($K^2 = (4\pi n/\lambda_D)^2 \sin^2(\theta/2)$) invariably exhibit curves of the same shape that was reported previously (16). Alternatively, one may plot $D_{app} \equiv \tau^{-1}/2K^2$ vs. K^2. A molecule with dimensions small compared to K^{-1}, such as poly(L-lysine) (degree of polymerization 955), at high ionic strengths will exhibit a constant D_{app} independent of K^2 over the accessible range, and the value of D_{app} will be simply that for translational diffusion of its center of mass. As shown in Figures 1 and 2, D_{app} for either native or pH-denatured DNA rises from its intercept at $K^2 = 0$ up onto a distinct plateau at large values of K^2. The upsweep in D_{app} represents the contribution from internal Brownian motion of the segments within the individual molecules, resulting in fluctuations of the internal interference factor. The existence of a distinct plateau demonstrates that internal Brownian motion simulates, or obeys, the free-particle diffusion equation with an effective segmental diffusion coefficient at large values of K^2.

A serious dilemma in understanding this behavior was finally resolved in 1976. The coupled bead-spring model of Rouse (17) and Zimm (18), especially the nondraining case treated by Zimm, was found by stopped-flow dichroism (19,20), zero-angle

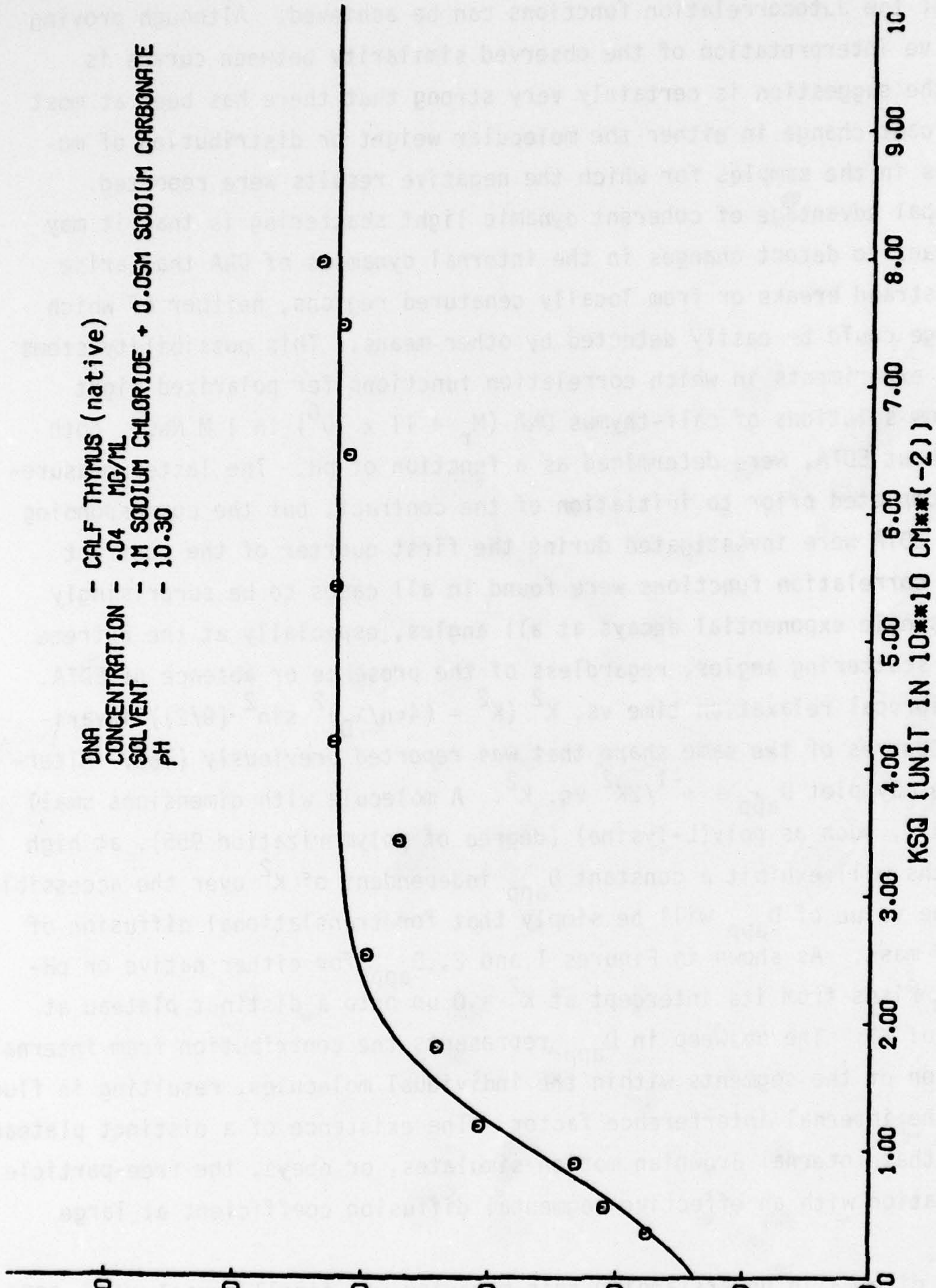

Figure 1. D_{app} vs. K^2 for native calf-thymus DNA.

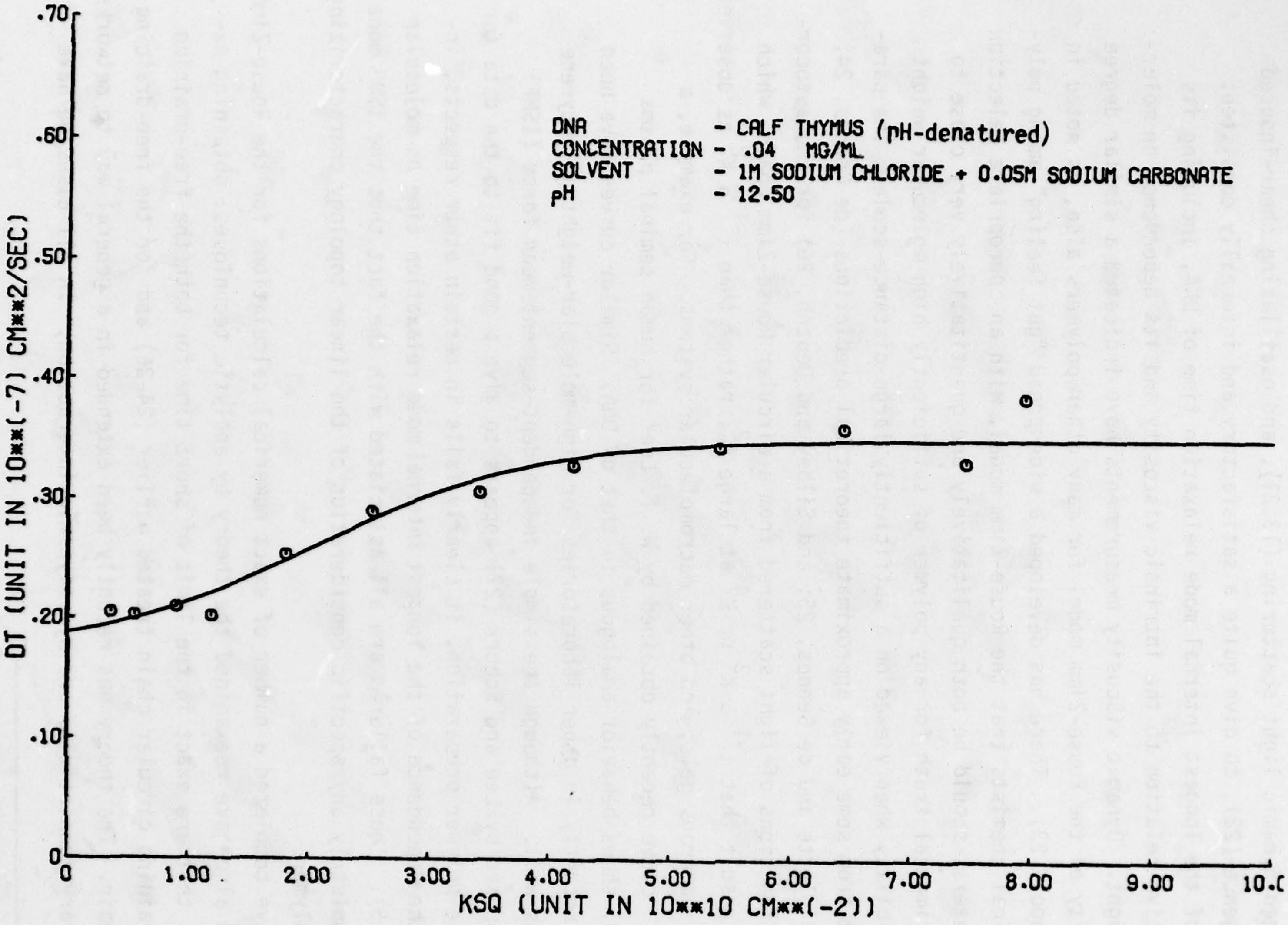

Figure 2. D_{app} vs. K^2 for pH-denatured calf-thymus DNA.

depolarized dynamic light scattering (13,21), and oscillating shear-induced birefringence (22), to give quite a satisfactory and internally consistent account of the longest internal mode relaxation time of DNA, including its quantitative relation to the intrinsic viscosity and its dependence on molecular weight. Dynamic viscosity measurements have indicated a similar degree of validity of the Rouse-Zimm model for many other polymers also, as noted in Ferry's book (23). There has developed a widespread "gut feeling" among polymer physical chemists that the Rouse-Zimm model, with an appropriate selection of parameters, should be both qualitatively and quantitatively very close to the experimental truth for any polymer of sufficiently high molecular weight and flexibility when viewed on a sufficiently large distance-scale. The paradox arose from some early approximate theoretical predictions (de Gennes, 24; du Bois-Violette and de Gennes, 25; and Silbey and Deutch, 26) for the autocorrelation functions of light scattered from a circular Rouse-Zimm chain, which gave the result that $\tau^{-1} \alpha K^3$ or K^4 at large K^2; rather than $\tau^{-1} \alpha K^2$ as observed for DNAs, numerous gels, and other macromolecular systems. For example, a τ^{-1} vs. K^2 curve recently obtained by W. I. Lee* for human seminal plasma (Figure 3) shows behavior analogous to that of DNA. Similar curves have been obtained recently in other laboratories for high-molecular-weight polystyrene samples as well. Although the simple independent-segment mean-force (ISMF) model proposed by Lee and Schurr (27) appears to give a good fit to the data for any single polymer preparation, it clearly fails in certain other respects, including the dependence of the longest internal mode relaxation time on molecular weight (15). These failures are all associated with the fact that the ISMF model omits completely any specific consideration of the linear topology characterizing a real polymer.

We have completed a number of exact numerical calculations for the Rouse-Zimm model and also have reexamined the theory by analytic techniques, obtaining expressions that are exact in the limit of short time for both the free-draining and nondraining circular chain treated earlier (24-26) and for the free-draining linear chain. The theory has recently been extended in a general way to networks of arbitrary connectivity and hydrodynamic interaction. In all cases we have

---

*Personal communication, W. I. Lee, Center for Bioengineering, University of Washington.

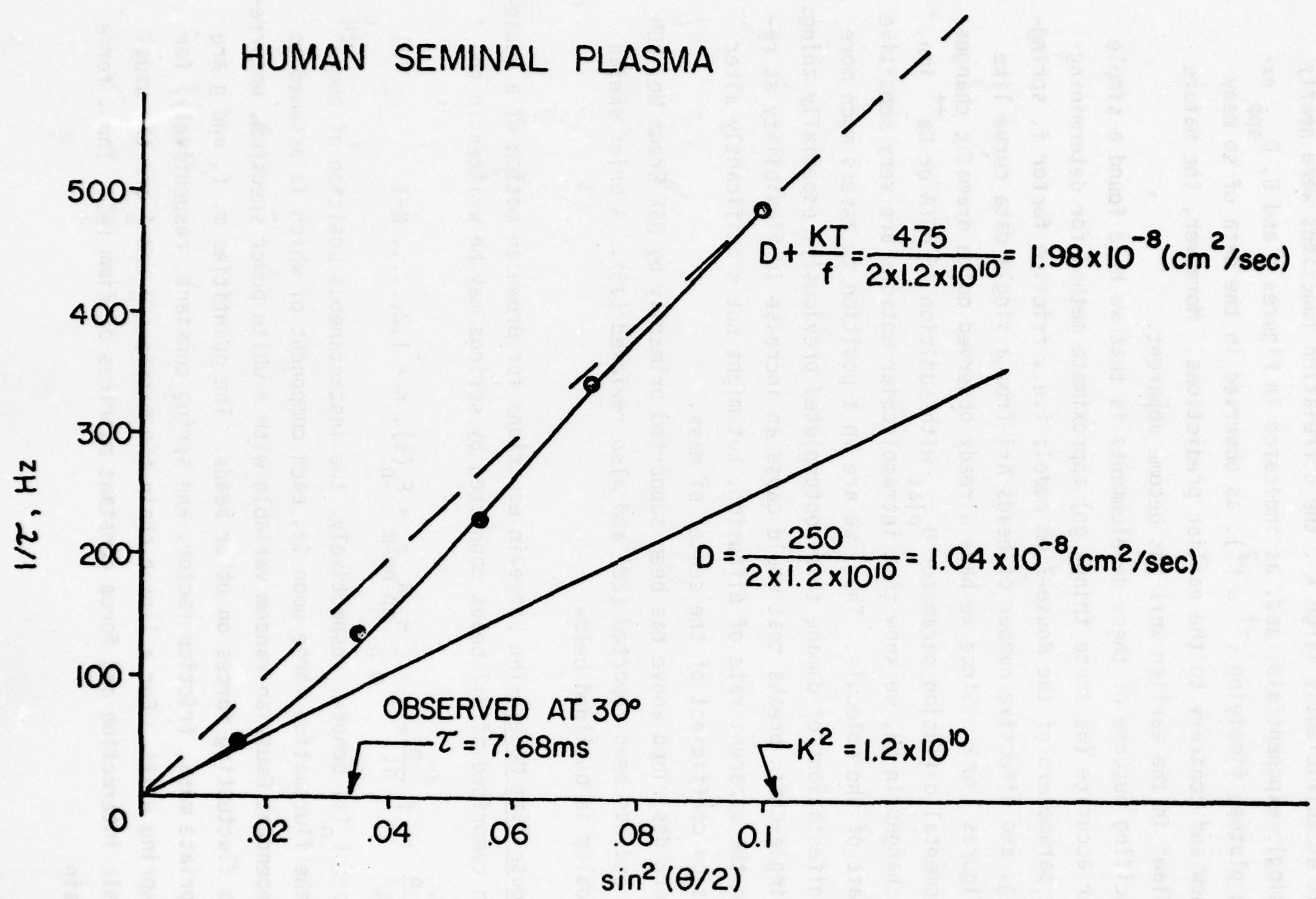

Figure 3. Reciprocal relaxation time vs. K^2 for human seminal plasma.

found that at sufficiently large K^2, the correlation functions were nearly perfect single exponentials; and, as indicated in Figures 4 and 5, D_{app} exhibited a plateau (implying $\tau^{-1} \alpha K^2$), as observed in the data of so many systems now and contrary to the earlier predictions. Moreover, the nature of the "flaw" in the earlier work has become apparent.

An exciting outcome of these developments is that we have found a simple and rather accurate (as these things go) approximate method for determining all these parameters of the Rouse-Zimm model; i.e., friction factor f, spring-constant g, and effective number of beads N+1 from a single data curve like that in Figures 1 or 2. Since we have already observed quite dramatic changes in the segmental diffusion parameter D_{plat} with addition of EDTA or Ca^{++} ion, and with changes in pH, we know that intramolecular motions are very sensitive to the state of the molecule. Thus, we are in a position to assess much more subtle manifestations of damage than contemplated previously, especially things such as single-chain breaks that would cause an increase in flexibility as reflected in the apparent rate of diffusion, but might not significantly alter the diffusion coefficient of the center of mass.

The work described above has been supported primarily by NSF Grant No. PCM 75-23631, and has been reported (28) and also reviewed (15). A brief sketch of the problem is outlined below.

<u>The Rouse-Zimm Model</u>--The Langevin equations for Brownian motion of a Rouse-Zimm chain comprised of N+1 beads connected by springs may be written in the form

$$m \frac{d^2 \underset{\sim}{r}_n}{dt^2} + f \frac{d\underset{\sim}{r}_n}{dt} + g \sum_m \sum_p H_{np} A_{pm} \underset{\sim}{r}_m = \underset{\sim}{F}_n(t), \quad n = 1,2,\ldots., N+1 \qquad (1)$$

where $\underset{\sim}{r}_n$ and $\underset{\sim}{F}_n(t)$ denote, respectively, the instantaneous position of the n^{th} bead and the fluctuating force upon it, each component of which is assumed to be an independent Gaussian random variable with a white power spectrum, uncorrelated with fluctuating forces on other beads. The quantities m, f, and g are the appropriate mass, friction factor, and spring constant, respectively, for the bead-spring units. For a linear chain the matrices $\underset{\approx}{H}$ and $\underset{\approx}{A}$ are the usual hydrodynamic interaction and force constant matrices of Zimm (4). Thus, for a linear chain

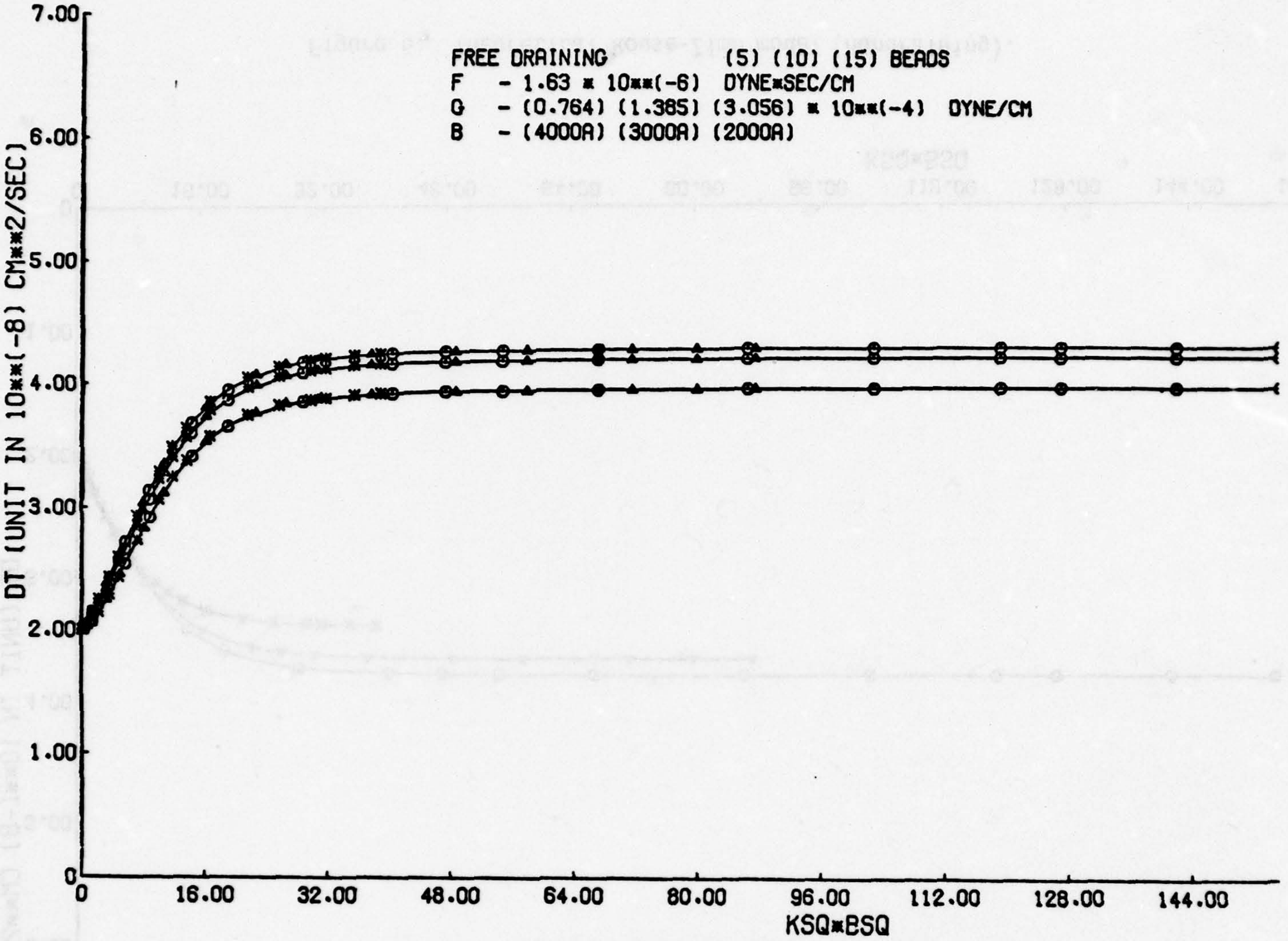

Figure 4. Theoretical Rouse-Zimm model (free draining).

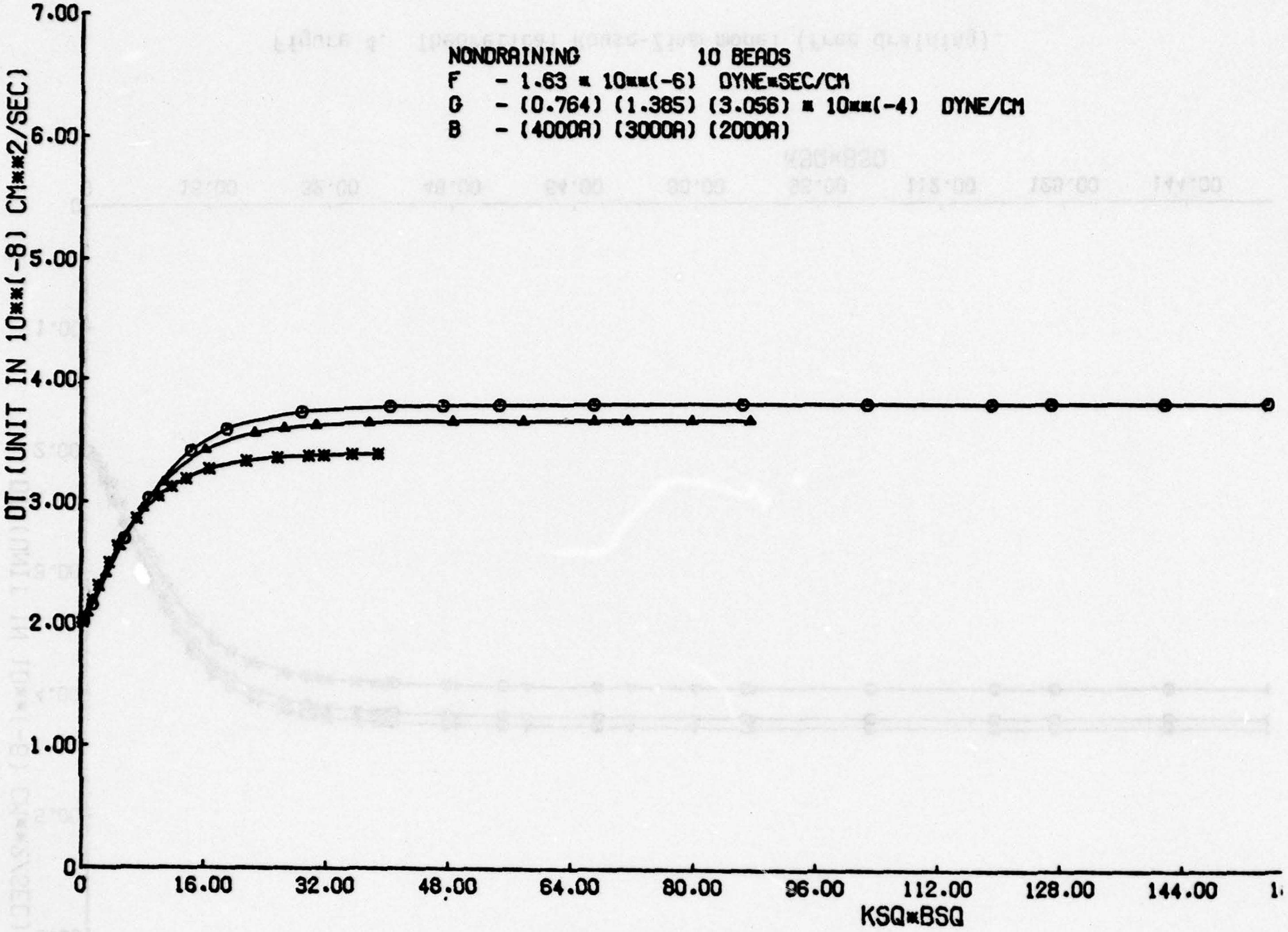

Figure 5. Theoretical Rouse-Zimm model (nondraining).

$$\underset{\approx}{A} = \begin{vmatrix} 1 & -1 & 0 & \cdots & & & 0 \\ -1 & 1 & -1 & 0 & \cdots & & 0 \\ 0 & -1 & 1 & -1 & 0 & \cdots & 0 \\ \cdot & & & & & & \cdot \\ \cdot & & & & & & -1 \\ \cdots & & & & 0 & -1 & 1 \end{vmatrix} \qquad (2)$$

and

$$H_{mk} = S_{m,k} + f[(6\pi^3)^{1/2}\,\eta b|m-k|^{1/2}]^{-1} \qquad (2b)$$

where η is the solvent viscosity and $b = (3k_BT/g)^{1/2}$ is the root-mean-squared spring extension, or separation between beads. After transformation to normal coordinates,

$$\underset{\sim}{\rho}_\ell(t) = \sum_{n=1}^{N+1} (Q^{-1})_{\ell n}\underset{\sim}{r}_n(t) \qquad (3)$$

a set of uncoupled Langevin equations for the normal modes results. The inertial terms may be ignored for all modes except the $\ell = 1$, or uniform mode, corresponding to the $\Lambda_\ell = 0$ eigenvalue of the product matrix $\underset{\approx}{H}\underset{\approx}{A}$, which is diagonalized by the similarity transformation $\underset{\approx}{Q}^{-1}\underset{\approx}{H}\underset{\approx}{A}\underset{\approx}{Q}$.

The autocorrelation function for the scattered electric field from a single polymer molecule at the detector is proportional to the intermediate scattering function defined by

$$G(k,t) \equiv \left\langle \sum_{n=1}^{N+1}\sum_{p=1}^{N+1} \exp\{i\underset{\sim}{K}\cdot[\underset{\sim}{r}_n(o) - \underset{\sim}{r}_p(t)]\}\right\rangle \qquad (4)$$

The autocorrelation function of the fluctuating intensity is proportional to $|G(K,t)|^2$. By a rigorous but lengthy argument, it can be shown (1) that

$$G(K,t) = e^{-K^2D_ot}\left\{\sum_{n=1}^{N+1}\sum_{p=1}^{N+1} \exp\left[-\frac{k^2}{2}\sum_{\ell=2}^{N+1} d_\ell^2\,(Q_{n\ell}^2 + Q_{p\ell}^2 - 2Q_{n\ell}Q_{p\ell}e^{-t/\tau_\ell})\right]\right\} \qquad (5)$$

where $\tau_\ell \equiv f/g\Lambda_\ell$ is the Langevin relaxation time of the ℓth normal mode, and Λ_ℓ is the ℓth eigenvalue of the nonsymmetric matrix $\underset{\approx}{H}\underset{\approx}{A}$.

Our computational algorithm consists of the following steps:

(1) Construct $\underset{\approx}{A}^{1/2}$ by elementary prescription;

(2) Construct the symmetric matrix $\underset{\approx}{A}^{1/2}\ \underset{\approx}{HH}^{1/2}$, which has the same eigenvalues as $\underset{\approx}{HA}$, and obtain its eigenvalues and normalized eigenvectors using a modified Household-Givens Sturm-sequence routine;

(3) Determine the eigenvectors of $\underset{\approx}{HA}$ from those of $\underset{\approx}{A}^{1/2}\ \underset{\approx}{HH}^{1/2}$ by a two-step procedure that avoids the difficulties associated with the fact that $\underset{\approx}{A}^{1/2}$ and $\underset{\approx}{A}$ are singular;

(4) The columns of Q are the eigenvectors of $\underset{\approx}{HA}$;

(5) When preserving the normalization indicated in step 3, $d_\ell^2 = \frac{K_BT}{g}$. The computation of G(K,t) readily follows.

Steps 1 - 4 of the above algorithm for determining the eigenvalues and normal modes of the polymer may prove useful for the computation of molecular deformations in shear fields associated with laser-induced shock waves, or of the strain of the intramolecular springs induced by hydrodynamic stresses on the macromolecule. A critical prerequisite for any such calculation, however, is an appropriate choice of the parameters f, g, and N+1.

On the basis of both analytic theory for the circular chain and computational results for the linear chain, an algorithm has been constructed for estimating the model parameters f, g, and N+1 from a single experimental curve of D_{app} vs. k^2. The development of this algorithm was comprehensively described in a recent communication (28), so it need not be detailed here. Remarkable variation of the model parameters with pH between 8.5 and 10.5 indicates that f and g are especially sensitive indicators of some kind of intramolecular dynamics, or flexibility. Our original hope that this same analysis might be used to study laser-pulse radiation-damaged DNA molecules has been thwarted by our inability to obtain unequivocal and reproducible damage at the power levels employed, except in one instance that appears increasingly spurious with the accumulation of further data. Still we remain optimistic that this Rouse-Zimm model analysis may blossom into a highly useful tool for assessing macromolecular damage, once we can reliably inflict the damage itself.

Theoretical Studies of Laser-Induced Damage in Macromolecules

Although unequivocal and reproducible evidence for laser-pulse-induced damage has not yet been obtained, some consideration has been given to possible damage mechanisms and how these might affect the distribution of damage-product sizes under different solution conditions.

At the outset one can distinguish three main classes of potential damage mechanisms: (a) laser-induced infrared photochemistry, (b) thermal and catalytic mechanisms, and (c) stress-induced mechanical strains. The first class of damage results simply from repeated excitation of specific modes, or groups of modes, that transfer the energy to other internal modes, thus heating the molecule up to the dissociation point, as reviewed recently by Bloembergen and Yablonovitch (29). The second class of damage arises from the catalytic effects of local heating or from hydrated electrons produced in dielectric breakdown, for example. The phosphate ester bonds in DNA are thermodynamically unstable with respect to hydrolysis; and at elevated temperatures (i.e., above 90°C), thermally induced bond cleavage proceeds at a significant rate. These first two classes of damage mechanisms would equally be likely to produce damage at any point in the DNA, irrespective of any naturally occurring structural inhomogeneities or conditions in solution, in a manner similar to ionizing radiation. For single-chain macromolecules, the distribution of product sizes is governed by the well-known Poisson distribution,

$$P(m) = \frac{a^m e^{-a}}{m!} \tag{6}$$

where a is the average chain length, which is inversely proportional to dose in the case of ionizing radiation. For double-stranded DNA, the complete scission of both chains requires two backbone "hits," or single-strand breaks, on opposite strands within some small number of base-pairs of one another. In that case, a varies quadratically with the dose in the initial phase, but the distribution of breakage-product lengths is still that of the Poisson distribution.

The third class of damage mechanisms includes all those in which mechanical strains of chemical bonds are developed in response to various kinds of stresses. The well-documented (30) cleavage of DNAs in the rather modest shear fields employed in both stirring and flowing operations of standard preparative procedures, suggests that the phosphate ester C-O backbone bond, site of more than 90% of this damage, is unusually predisposed to scission under tensile strain. The tensile force required, however, is an order of magnitude less than the bond-dissociation energy. Moreover, the enormous activation energy observed for this shear-induced cleavage process is comparable to the bond-dissociation energy, suggesting that it is primarily a strain-catalyzed hydrolysis reaction rather than an outright bond rupture. There is, then, the definite possibility that certain of the backbone bonds in DNA, in particular the phosphate ester C-O bonds, may be unusually susceptible to strain-induced cleavage by laser-pulse-induced stresses, although a picosecond laser pulse might not allow adequate time for the hydrolytic step to proceed. It is entirely possible that a train of picosecond pulses extending over hundreds of nanoseconds or more may develop a strain of sufficient duration to allow the catalysis to proceed, even when a single picosecond pulse of much higher power has no effect. This is a mechanism in which a threshold in time duration as well as pulse power may be observed.

Various possible stresses induced by high-intensity optical fields come to mind. The induction of shock waves in media by laser pulses is well established, and the latter could contribute both substantial transient heating and viscosity-coupled tensile stresses on the macromolecule. Dielectrophoresis of a macromolecule with dielectric constant differing from that of the solvent can be induced by a.c. electric fields that exhibit spatial gradients. For high-power pulses, especially in situations where filament formation occurs, the field gradients may be substantial and therefore capable of inducing dielectrophoretic tensile-strain-induced cleavage.

Strains resulting from optically induced torques are also likely candidates for the mechanism of laser-pulse-induced damage. Optically induced orientation of small molecules is a well-documented phenomenon. Indeed, it has been exploited to considerable advantage locally by A. P. Bruckner (31, 32) in his work with the range-gated carbon disulfide picosecond shutter. The carbon disulfide molecule S = C = S exhibits a significantly greater optical polarizability, α_{11}, along the axis of the molecule than that, $\alpha_{\perp}$, in the transverse plane. If the axis of such a molecule makes an angle θ with respect to the direction of the optical electric field $E(t) = E_o \cos(\omega t)$, then the instantaneous polarization energy is $U(t) = \frac{E(t)^2}{2}[\alpha_{11}\cos^2\theta + \alpha_{\perp}\sin^2\theta]$. The time-average polarization energy may be expressed as

$$\overline{U} = \frac{E_o^{\,2}}{4}\left[\alpha_o^{\,2} + (\alpha_{11} - \alpha_{\perp})\left(\cos^2\theta - \frac{1}{3}\right)\right] \tag{7}$$

where $\alpha_o = 1/3\,(\alpha_{11} + 2\alpha_\perp)$ is the isotropic polarizability, and $\alpha_{11} - \alpha_\perp$ is the anisotropy of the polarizability. The resultant torque on the molecule is simply

$$\frac{\partial \bar{U}}{\partial \theta} = \frac{E_o^2}{4} (\alpha_{11} - \alpha_\perp)\, 2 \cos\theta \sin\theta \tag{8}$$

from which it can be deduced that the torque will be maximal when the molecular axis is oriented at 45° to the field. Any small molecule with a significant optical anisotropy will orient in a sufficiently intense optical field. This is just the standard optical Kerr effect.

A polymer comprised of monomer units, each of which exhibits an optical anisotropy, will be strained in an intense optical field as a consequence of the simultaneous response of all the subunits to the applied torque on each element. Macromolecules exhibit form optical anisotropy, due to the shape-related anisotropy of the internal field, as well as intrinsic optical anisotropy of the bonds or monomer units. Only the latter anisotropy contributes to the torque-induced strain discussed below.

The question addressed here is the strain and distribution of strain induced by optical torques on a rodlike polymer or rodlike section of a much larger polymer. A greatly exaggerated strained version of a simple polymer model is indicated in Figure 6. In all, the polymer contains N (even) monomer units, each of which is optically anisotropic; and for simplicity, the strain is assumed to reside entirely in the springs (of zero equilibrium extension) that preserve alignment of the monomer axes in the unstressed situation. The basic ansatz is that of conventional Brownian motion theory in which the externally applied torques and forces are instantaneously balanced by viscous forces on the elements moving through the solvent fluid. This may not be a reasonable procedure on the picosecond time scale, but it is a beginning. Denote the extension in the x-direction of the spring connecting the n and n+1 beads by $S_{n,n+1}$. The torque T_n on the nth bead is balanced by that of its springs, thus

$$T_n = -g\,\frac{a}{2}\,[S_{n,n+1} + S_{n-1,n}] \tag{9}$$

where g is the Hook's law spring constant and a is the distance between monomer

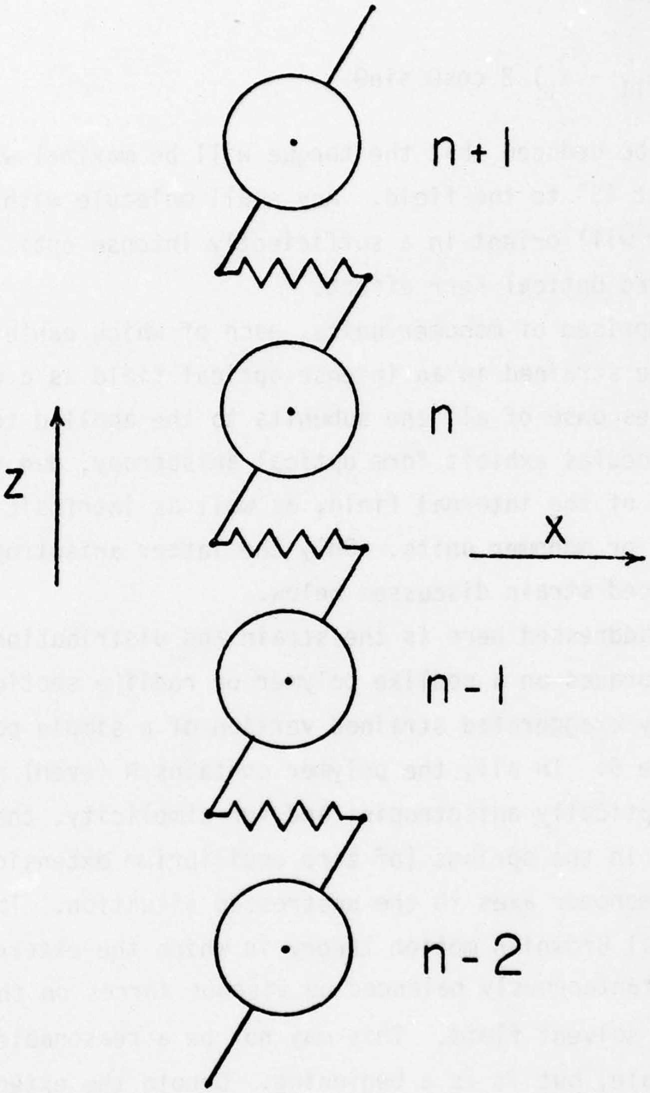

Figure 6. Schematic of simple polymer model used in analysis of EM torque-induced breakage of DNA.

centers. We will make use of the fact that most real chemical bonds rupture at rather small deformations; so if the polymer is intact (i.e., no bonds have ruptured), the actual monomer axes make only a negligibly small angle with the axis of the rod, in which case the torques on the various monomers are for practical purposes identical and equal to

$$T = \frac{E_o^2}{4}(\alpha_{11} - \alpha_{\perp})\, 2 \cos\theta \sin\theta \tag{10}$$

where θ is the angle between the rod axis and the optical electric field. As a consequence of the total torque on the polymer, the entire rodlike array will rotate about its center with angular velocity $\dot{\theta}$. This rotation of the rod in a direction to minimize the external torque is opposed by the Stokes friction of the monomer units travelling through the resting solvent. The hydrodynamic drag force F_n on the nth monomer bead is likewise balanced by its spring forces, thus

$$F_n = f(n - \frac{N+1}{2})a\dot{\theta} = g(S_{n,n+1} - S_{n-1,n}),\ n \geq \frac{N}{2} + 1 \tag{11}$$

where f is an appropriate Stokes law drag coefficient, and $(n - \frac{N+1}{2})a\dot{\theta}$ is the linear velocity in the x-direction of the nth monomer through the fluid due to overall rotation of the rod. The quantity $S_{n-1,n}$ can be eliminated by combining equations 9 and 11 to give

$$S_{n,n+1} = f(n - \frac{N+1}{2})\frac{a\dot{\theta}}{2g} - \frac{T}{ga} \tag{12}$$

There exists also a relation between the angular velocity of the array and the total torque on the array, that is

$$T_{tot} = NT = f_{\Omega}\dot{\theta} \tag{13}$$

where f_{Ω} is the friction factor for rotation of the array. The quantity T_{tot} can also be computed under the same hypothesis of Stokes drag on the monomers that was employed above, thus

$$T_{tot} \simeq 2 \sum_{n=\frac{N}{2}+1}^{N} [f(n - \frac{N+1}{2})a\dot{\theta}]\,[(n - \frac{N+1}{2})a] = f_{\Omega}\dot{\theta} \tag{14}$$

where the first factor in the sum represents the hydrodynamic forces on the monomers, and the second gives the lever-arm of each. Setting $n - \frac{N+1}{2} = m + 1/2$, where $m = n - (\frac{N}{2} + 1)$, one obtains

$$f_\Omega \simeq 2\,a^2 f\,[\sum_{m=1}^{\frac{N}{2}-1} (m + \tfrac{1}{2})^2] \tag{15}$$

$$\simeq 2\,a^2 f\,[\frac{N^3 - N + 20}{24}]$$

Using equations 13-15 in equation 12 gives

$$S_{n,n+1} = \frac{-T}{ga}\,[1 - \frac{6(n - \frac{N+1}{2})}{N^3 - N + 20}],\; n \geq \frac{N}{2} + 1 \tag{16}$$

This equation gives the extension, or strain, in any spring except for the first and last, which will be less by about a factor of 2. (End effects have been neglected here.) The maximum strain is developed in the springs of the central monomers at $n = N/2$, $N/2 + 1$. However, for a large number N of monomers comprising the rod, the second term in brackets is negligible for any value of n, so the strain will be essentially the same in all springs regardless of n, except for the first and the last. Even for N as small as 4, the maximum value of the last term for $n = 4$ would be only 0.112; for $N = 10$, it is 0.027. Thus, in practice one can expect the strain to be instantaneously distributed over all springs essentially uniformly. If the solvent should be rigid rather than viscous on the 10^{-12}-sec time scale, then the strain will be exactly the same in all springs, ignoring the end effects. Moreover, the strain is likewise independent of N for $N \gtrsim 4$.

From the above results one sees that for a given orientation of the rodlike polymer, the strain induced by the optical torque is: (a) proportional to E_o^2, or the pulse intensity, (b) nearly uniformly distributed over the rod, and (c) essentially independent of N for $N \gtrsim 4$. Thus, for a rod of a given orientation, this mechanism predicts sharp threshold behavior. Below a critical intensity, none of the bonds break; and 20% above the critical intensity, the rod breaks completely down to pieces with $N < 4$. In any given solution not all rods have the correct orientation to provide the critical torque. The distribution of breakage products will consist of unbroken whole rods and a large number of very small pieces from those that exhibited the proper orientations. For a semiflexible macromolecule such as DNA, any one molecule will at the instant of exposure be comprised of some segments that have the proper orientation and some that don't. The axial orientation of the DNA is believed to change relatively little over some fraction of a persistence length, say over 5-10 nm. Thus, one might expect to find some large fragments up to this size or a few times larger, plus a great many much smaller pieces, when operating 20-50% above the threshold.

The distribution of breakage products for the simple optical torque mechanism differs substantially from that which obtains from either direct IR pumping or catalytic mechanisms.

DNA is believed, from various lines of evidence, to contain a small number of structural inhomogeneities, or fluctuations, the number of which is pH dependent. These features would be expected to provide weak spots that are more susceptible to breakage under tensile stress (as is the case for single-strand polynucleotides); but, owing to their flexibility, they should actually be more stable against optical torques. Thus, the observation of a strong pH dependence of the breakage process would implicate tensile stresses rather than optical torques.

These simple ideas can be generalized to other more realistic models, and at least some of the pertinent parameters can be readily estimated. For example, the optical anisotropy can be estimated from the cross-section for depolarized scattering, although separation of the contributions of intrinsic and form anisotropy may require some educated guessing. Nonetheless, the conclusions do indicate that it may be possible to eliminate some classes of damage mechanisms if the entire product distribution can be measured.

EXPERIMENTAL FACILITIES

Ultrashort laser-pulse-induced damage studies of calf-thymus DNA, the synthetic polypeptide poly(L-lysine), and other macromolecular systems are carried out using a Nd:Glass laser system capable of single- and multiple-pulse operation. Damage in the macromolecular samples is monitored principally by the technique of dynamic light scattering. The experimental apparatus developed for these studies is described in this section.

The Picosecond Laser Irradiation Facility

The ultrashort-pulse laser facility assembled for the purpose of irradiating selected macromolecular samples is illustrated in Figure 7. It consists of five subsystems: the mode-locked Nd:Glass laser, the high-speed Pockels cell pulse-switching system, the pulse chronometer and video detection system, the irradiation target cell, and the pulse-energy measurement system. Each of these is described below.

The Nd:Glass Laser--The mode-locked Nd:Glass laser (33) consists of a water-cooled, Brewster-angled, Owens-Illinois ED-2 glass rod, 1.3-cm dia x 22.9-cm length, pumped by two EG&G linear flashlamps in a double elliptical reflector cavity. The resonator is formed by a flat 99.7% rear reflector (M_1) and a 10-m radius 35% output reflector (M_2). Mode locking is accomplished by a flowing 1-mm-thick dye cell placed in direct contact with the rear reflector. The dye solution consists of Eastman 9860 dye in dichloroethane at a concentration that results in a small signal-transmission factor of $\sim$60% at 1060 nm. An iris diaphragm (ID_1) is used to control transverse mode size and purity. By closing it down to an aperture of 6-mm dia or less, TEM_{00} output can be obtained. In the above configuration the laser produces a train of $\sim$100 horizontally polarized pulses at λ = 1060 nm, each of 10-20-psec duration and >100-MW peak power, spaced at 5.6-nsec intervals (the round-trip cavity time).

The choice of dye cell geometry is critical to laser performance. We have experimented with various types of discrete dye cells and with the contacted type, with and without dye circulation, and have found that the circulating contacted cell produces the most consistent and reproducible pulse trains, with excellent suppression of satellite pulses. Beam stability and mode purity are also optimized with this configuration.

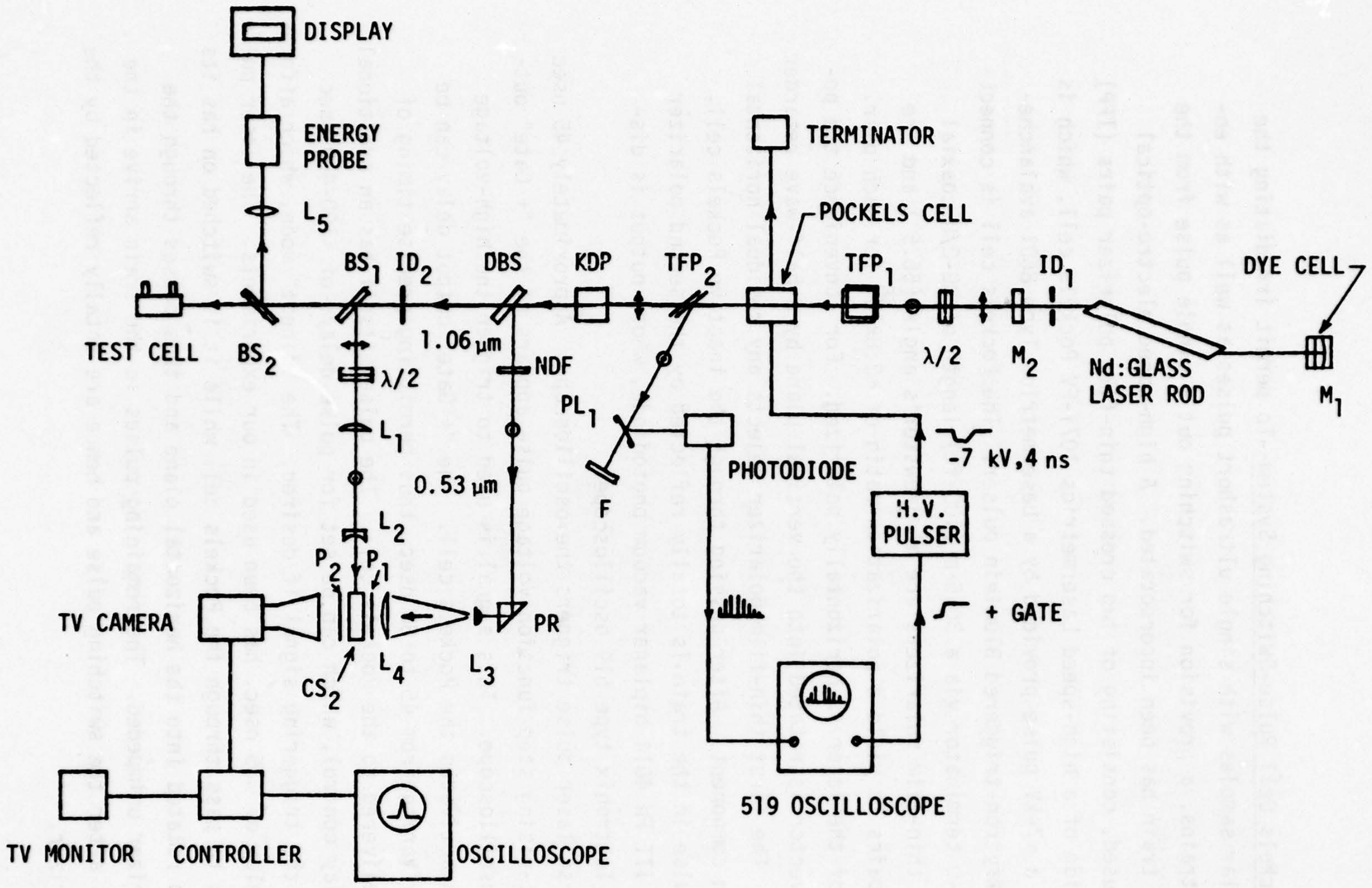

Figure 7. Schematic of apparatus for picosecond laser irradiation of macromolecular systems.

The Pockels Cell Pulse-Switching System--To permit irradiating the macromolecular samples with single ultrashort pulses as well as with entire pulse trains, a provision for switching out a single pulse from the mode-locked train has been incorporated. A high-speed electro-optical shutter is used, consisting of two crossed thin-film polarizer pairs (TFP) on either side of a high-speed Lasermetrics 1071-FV Pockels cell, which is switched by a ∿7-kV pulse provided by a Lasermetrics Type 8601 avalanche-transistor krytron-triggered Blumlein pulser. The Pockels cell is connected to a 50-Ω terminator via a 30.5-m (100-ft) length of RG-8/U coaxial cable. The thin-film polarizers are at Brewster's angle (56.5°) and are stacked in pairs to yield a polarization ratio of $\sim 2.8\times10^5$ for each pair. The output of the laser is horizontally polarized. For convenience the polarization vector is rotated into the vertical plane by a half-wave retarder plate, $\lambda/2$. The first thin-film polarizer rejects any residual horizontal polarization component. After passing through the inactive Pockels cell, the first pulse in the train is totally reflected by the second polarizer stack to an ITT FW 4014 biplanar vacuum photodiode, whose output is displayed on a Tektronix type 519 oscilloscope.

The first laser pulse triggers the oscilloscope. Approximately 45 nsec later a fast-rising step function voltage pulse appears at the "+ Gate" output of the oscilloscope. This signal is used to trigger the high-voltage pulser which activates the Pockels cell. The "+ Gate" output delay can be continuously varied from 45 to 80 nsec, thus permitting precise timing of the pulse delivered to the Pockels cell. The pulser itself has an additional variable-delay control, which can be set for pulse delays of ∿100-400 nsec relative to the triggering signal if desired. The "direct" mode, which affords a shorter delay of ∿35 nsec, has been used in our experiments. The laser pulse that happens to pass through the Pockels cell while it is switched on has its polarization rotated into the horizontal plane and thus passes through the second polarizer unimpeded. The remaining pulses in the train arrive in the Pockels cell after the switching pulse and hence are totally reflected by the second polarizer.

We have been able to switch out clean single pulses with up to 90% efficiency, with a good degree of reproducibility. Generally, about 3 out of 5 shots are successful (i.e., >70% throughput with no measurable bleed-through of adjacent pulses), provided the mode-locked pulse train is devoid of any spurious or satellite pulses which could cause premature triggering. Figure 8a displays the pulse shape delivered by the high-voltage pulser. It has a rise time of ∿1.5 nsec and full width at half-maximum of ∿4 nsec. The Pockels cell has a subnanosecond risetime and an extinction ratio of ≃1400 at 1060 nm. Figure 8b shows a typical, clean, mode-locked pulse train of about 100 pulses, with a single pulse extracted at about 90 nsec from the beginning.

<u>The Pulse Chronometer System</u>--Temporal width measurement of the selected ultrashort pulse is carried out by means of a picosecond streak shutter that we have used extensively in other work (31,32). The selected single pulse generates second harmonic light (530 nm) in a KDP crystal tuned to yield an SHG conversion efficiency of about 1%. The superimposed infrared (IR) and green pulses are separated at the dichroic beam splitter (DBS) (Fig. 7). A 50% beam splitter (BS_1) directs half the IR pulse energy to the ultrafast streak shutter. The polarization of this pulse is rotated into the vertical plane by a half-wave retarder, $\lambda/2$. Lenses L_1 and L_2 reduce the beam diameter by a factor of four. The pulse then traverses a quartz cell filled with carbon disulfide (CS_2). This cell is located between two high-quality crossed polarizers (P1, P2) whose axes are at 45° to the horizontal. These three components constitute the ultrafast streak shutter. As it travels through the CS_2, the IR pulse induces a narrow zone of birefringence in its immediate vicinity (34). To an observer viewing the shutter at right angles to the IR path, the effect is that of a narrow slit moving across the line of sight at the speed of light in CS_2 (1.84×10^{10} cm/sec). The shutter thus produces a streak record of light pulses incident at right angles to the IR path.

The green pulse split-off at the dichroic beam splitter is directed toward the shutter by a right-angle prism (PR) and expanded horizontally by a pair of cylindrical lenses (L3, L4) to illuminate the entire length of the

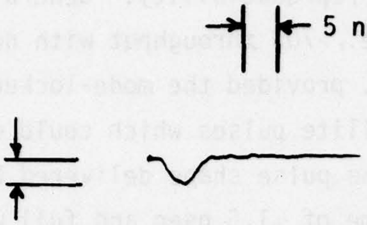

a) Pulse delivered by high-voltage pulser.

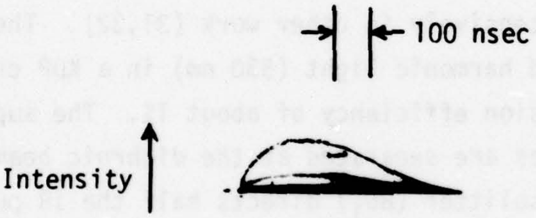

b) Mode-locked pulse train with single pulse switched out ~90 nsec from beginning.

Figure 8. Characteristic outputs of high-voltage pulser and mode-locked glass laser.

shutter, where it is sampled by the IR gating pulse. The signal exiting from the shutter is a cross-correlation between the gating and green pulses (35,36). If the depth of the IR gating pulse is small, it can be shown that the transverse dimension of the transmitted green pulse is essentially the same as the geometrical pulse length of the IR pulse in air.

The pulses gated by the shutter are detected by the video detection and display system (VDDS) shown in Figure 9 (31,32). The shutter output is imaged by a Telemation TMC-1100 CCTV camera equipped with an RCA 4532A silicon vidicon tube. The video signal is processed by the video display control unit (VDC) and displayed on an RCA CCTV monitor. Superimposed on the display is a bright rectangular frame generated by the VDC. The frame height can be varied from 1 to 64 TV lines, and its width from an equivalent of 64 lines to full screen width. The intensity profiles of the TV lines within the frame are displayed on an oscilloscope.

The VDDS is operated in the single-shot mode, wherein only a single sweep of the vidicon and display oscilloscope occurs. In this case only half the field of TV lines is swept; i.e., only the odd- or even-numbered lines. This avoids charge leakage from the transient image on the vidicon in the time between sweeps of the odd and even fields. Thus, in this mode up to 32 alternate lines can be examined. A trigger output pulse from the VDC fires the laser at the start of the vidicon sweep.

A typical example of ultrashort-pulse chronography obtained with this system is shown in Figure 10. Two pulse displays are shown superimposed. In each case only 3 TV lines through the center of the gated pulse were scanned. The B pulse was obtained by introducing a 14.8-psec delay in the green path by means of a 10-mm-path quartz spectrophotometric cell (1.25-mm wall) filled with water. The horizontal scale represents time; the vertical scale, intensity. The spatial separation of the two recorded pulses calibrates the system. On the recording film, 1 mm corresponds to 3.3 psec. Thus we see that pulses A and B appear to have half-widths of ∿17.5 psec and ∿16.5 psec, respectively. Accounting for the finite thickness of the birefringent zone in the CS_2 (∿1.5 mm), the pulse durations actually turn out to be about 15% lower--14.9 psec and 14 psec, respectively.

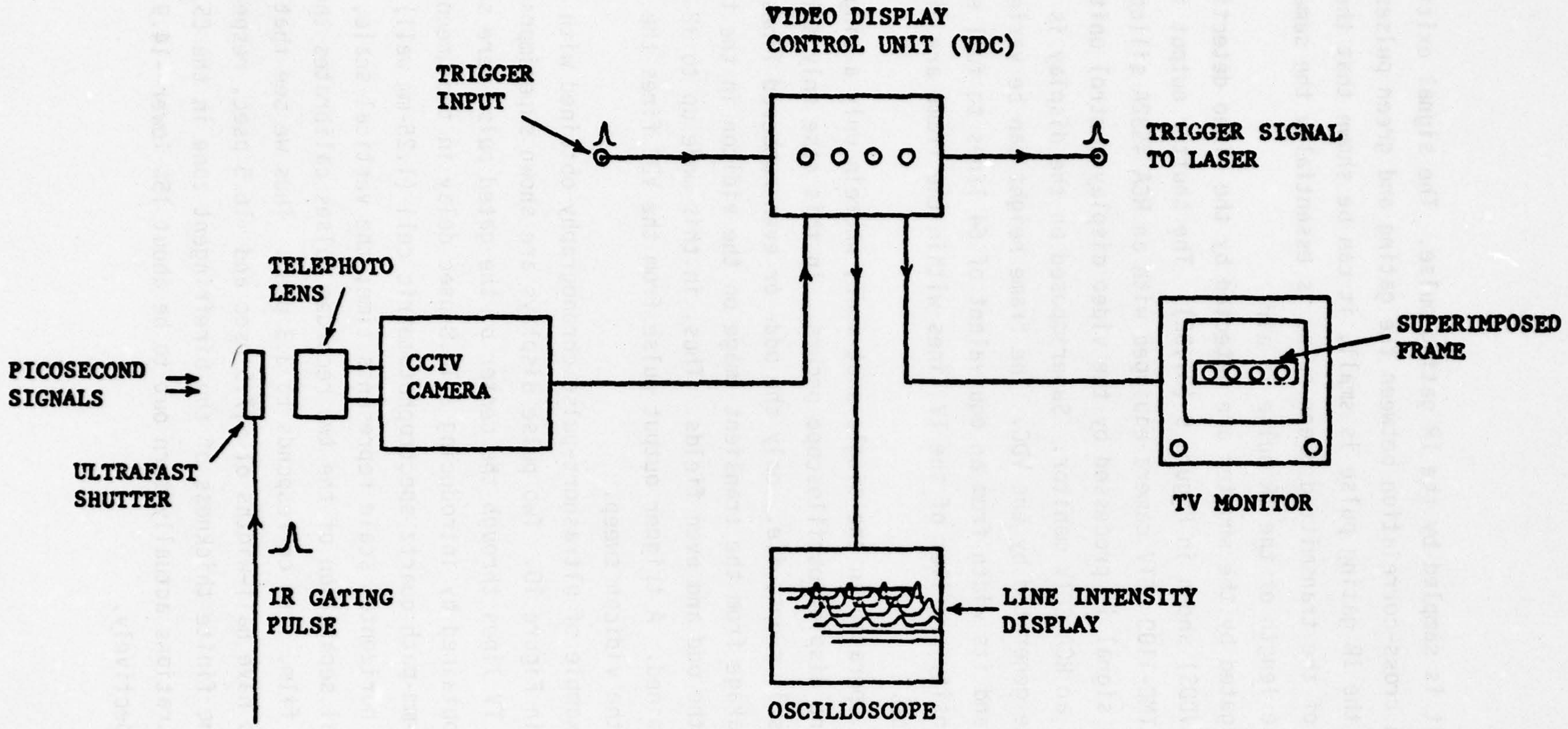

Figure 9. Schematic of video detection and display system (VDDS).

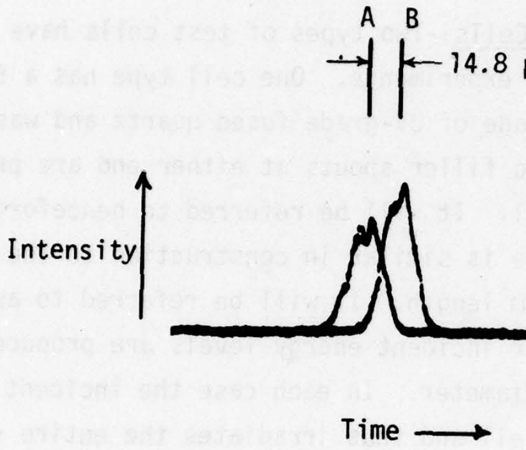

Figure 10. Ultrafast chronography of two laser pulses separated by 14.8 psec.

The VDDS can also be used to measure the beam spatial profile. When the ultrafast shutter and the cylindrical lenses are removed, the green pulse impinges directly on the vidicon tube. Since the green-pulse spatial profile is proportional to the square of the IR profile, any departures from the Gaussian TEM_{00} mode are immediately apparent.

The Irradiation Sample Cells--Two types of test cells have been manufactured for the irradiation experiments. One cell type has a 5-mm ID and a 2-cm path length. It is made of UV-grade fused quartz and was constructed by Precision Cells, Inc. Two filler spouts at either end are provided for filling and flushing the cell. It will be referred to henceforth as the "short" cell. The other type is similar in construction to the short cell but has a 2-mm ID and a 10-cm length. It will be referred to as the "long" cell. It is used when higher incident energy levels are produced by focusing down the incident beam diameter. In each case the incident laser pulse just fills the bore of the cell and thus irradiates the entire sample.

Pulse Energy Measurement--The IR laser pulse energy is monitored by a laser Precision RkP-331 pyroelectric energy probe and Rk-3230 digital display unit. This system was calibrated by the manufacturer using standards traceable to the National Bureau of Standards. A 20-cm-focal-length (f.l.) lens placed 10 cm in front of the probe focuses the incident IR pulse to <3-mm dia for acceptance by the probe aperture. The incident pulse is sampled by means of an uncoated glass beamsplitter (BS_2 in Fig. 1).

The Dynamic Light Scattering Facility

The dynamic light scattering apparatus consists of a CW He-Ne laser operating at 632.8 nm with approximately 50 mW power, the optical detection system, photon counting and correlating electronics, and a PDP-12 computer for data analysis and storage. The block diagram of the experimental setup is shown in Figure 11. The laser and optical detection system are mounted on a vibrationally damped table which consists of a 1360-kg, 3.7-m-long, 84-cm-wide-flange, steel I-beam sitting upon 16 free-floating springs grouped into four groups of four. The resonance frequency of the beam with respect to the floor is between 1 and 2 Hz, as per design.

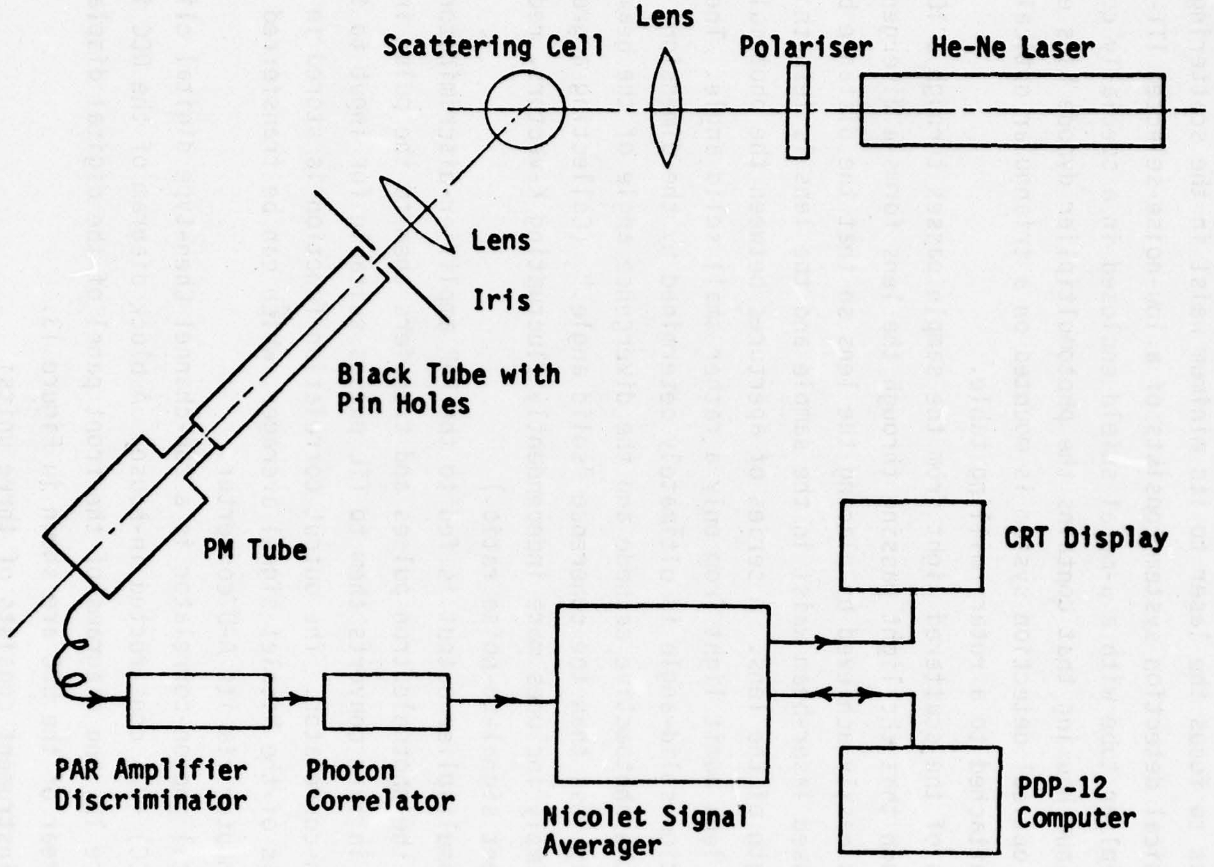

Figure 11. Experimental arrangement for dynamic light scattering.

The output of the laser is passed through an optical polarizer and a 10-cm-f.l. lens to focus the laser to its minimum waist in the scattering cell. The optical detection system consists of a low-noise-selected ITT-FW 130 photomultiplier tube with a μ-metal shield enclosed in a specially constructed aluminum housing that contains the photomultiplier dynode bias electronics. The optical detection system is mounted on a triangular optical rail rigidly attached to a rotary milling table.

A portion of the scattered light from the sample passes through a 10-cm lens placed such that the light passing through the lens forms a divergent cone. This is easily achieved by placing the lens so that the distance between the focused laser-beam waist in the sample and the lens is less than the focal length of the lens. A series of apertures between the photomultiplier and the lens admit light from only a rather small solid angle. The actual collection solid-angle is ultimately determined by the dimension (0.25 mm) of the photoactive cathode and the divergence angle of the beam, and is slightly less than the coherence "solid angle." (Collecting a greater solid angle simply includes more independently fluctuating $\underset{\sim}{K}$-vectors, reducing the apparent signal-to-noise ratio.)

The photomultiplier output is fed to the PAR amplifier-discriminator, which selects the photoelectron pulses and transfers them to the pulse inverter. This in turn converts them to TTL pulses suitable for input to the digital photon-correlator. The output correlation function is stored in the memory channels of the Nicolet signal averager, which can be transferred to the PDP-12 computer via its A-D converter.

The digital photon-correlator is a 256-channel Chen-type digital clipped correlator (DCC) (37) constructed in-house. A block diagram of the DCC is shown in Figure 12, and diagrams of the front panel of the digital display unit and the rear of the DCC are shown in Figure 13.

The DCC instrument consists of three units:

(1) Electronics Chassis. A 19-slot card cage which contains 16 correlator boards, a clock-control board, a clipper-scaler board, and a counter-display board. All active circuitry is contained in this box. The Electronics Chassis has six connectors:

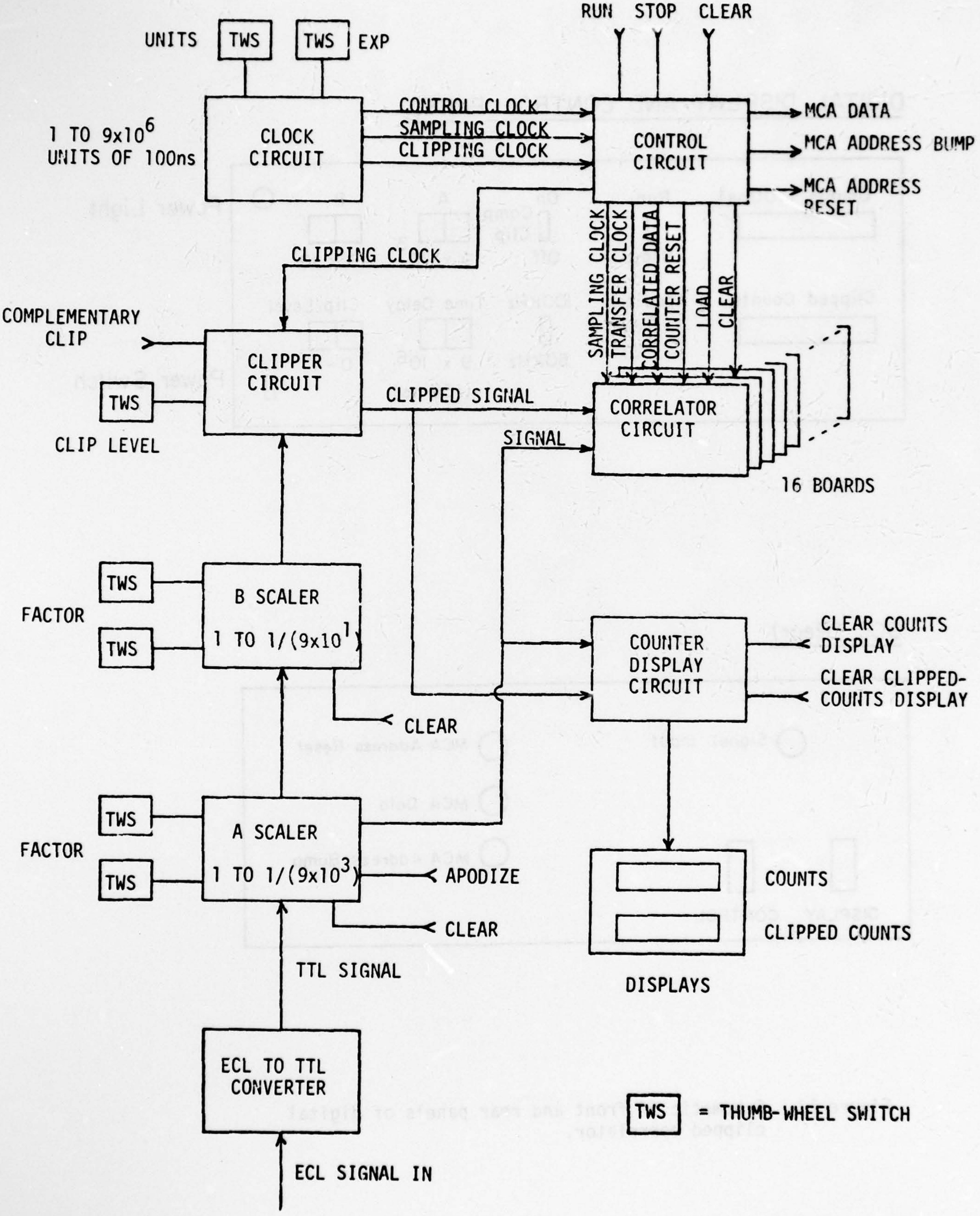

Figure 12. Block diagram of digital clipped correlator.

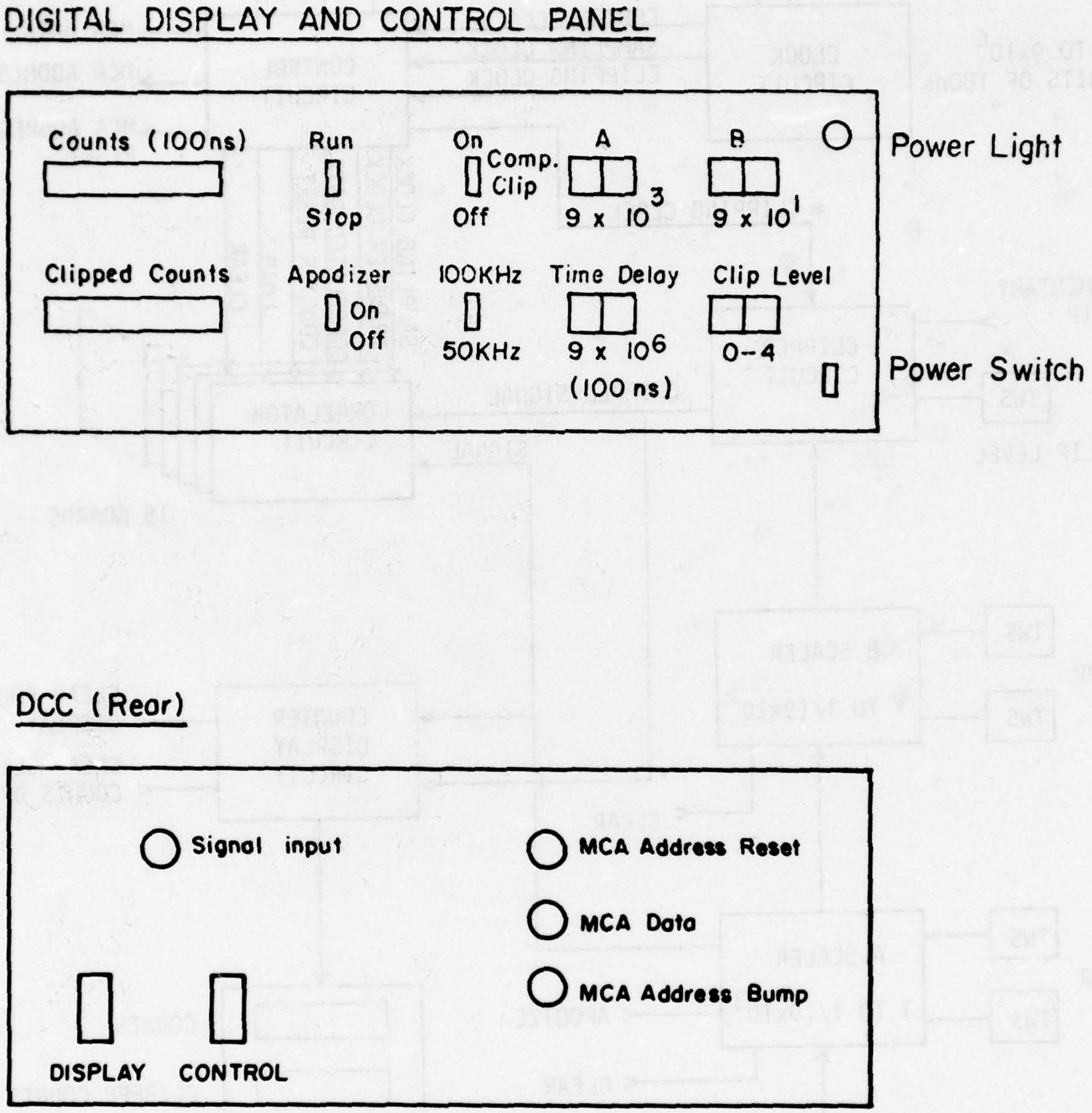

Figure 13. Schematic of front and rear panels of digital clipped correlator.

(a) Display - A 24-pin Elco connector that carries the multiplexed display signals and the display reset lines.

(b) Control - A 33-pin Elco connector that carries the control signals from the display and control panel.

(c) Signal Input - A BNC connector that carries an ECL level pulse from the amplifier discriminator.

(d) MCA Address Bump - A BNC connector that carries a pulse which increments the MCA channel address, generating a sweep.

(e) MCA Address Reset - A BNC connector that carries a pulse which resets the MCA channel address to zero, in preparation for another sweep.

(f) MCA Data - A BNC connector that carries a pulse which causes the MCA to increment the value stored at the currently addressed channel.

(2) Display-Control Chassis. This box contains a negative voltage power supply for the ECL to TTL converter, auxiliary power outlets for the logic power supply and fan, and the following control and display devices:

(a) On-Off thumbwheel switch (TWS) - applies line power to the instrument.

(b) Pilot light - indicates presence of line power to instrument.

(c) Run-Stop switch - causes control circuit to generate signals used by correlator boards and MCA.

(d) Apodizer switch - stops flow of signal to correlator boards, but allows clipped signal to shift down correlators.

(e) Complementary Clipping switch - causes a logical "1" to be shifted into correlators if clipping level is <u>not</u> exceeded during a correlation interval.

(f) System Clear switch - resets all counters in the system to zero (except display counters), and presets the control circuit for the next correlation run.

(g) Counts Display Clear switch - clears counts display.

(h) Clipped Counts Display Clear switch - clears clipped counts display.

(i) Clock Circuit TWS - a 2-digit (units and exponent) thumbwheel switch that selects the correlation interval over the range 1 to 9×10^6 in units of 100 ns.

(j) A-Scaler TWS - a 2-digit (units and exponent) switch that selects the scaling factor over the range 1 to $1/(9 \times 10^3)$.

(k) B-Scaler TWS - a 2-digit (units and exponent) switch that selects the scaling factor over the range 1 to $1/(9 \times 10^1)$.

(l) Clipping Level TWS - a 1-digit switch that selects the number of counts that must be exceeded during a correlation interval in order to cause an output from the clipper circuit.

(m) Counts Display - a 7-digit display of total counts output from the A scaler.

(n) Clipped Counts Display - a 7-digit display of total clipped counts output from the clipper circuit. Also acts as pilot light for 5-V logic supply.

(3) Power Supply. A +5-V logic power supply which delivers approximately 20 A to the DCC.

EXPERIMENTAL PROTOCOL

Poly(L-lysine)

The poly(L-lysine) was dissolved in water to a ratio of 10 mg/ml. Part of this solution was used to fill the short sample cell for irradiation by the IR laser pulses. The cell was filled carefully to minimize the occurrence of air bubbles at the optical windows or in the optical path of the laser pulse. Air bubbles inside the optical cell could cause significant scattering of the incident laser pulse, thus introducing errors in our measurements. Sometimes the optical cell had a few microscopic-size air bubbles attached to the peripheral side of the exit window. The bubbles were attached to the cell surface with no freedom to move; therefore, it is expected that these microscopic air bubbles did not introduce any error.

The poly(L-lysine) solution in the optical cell was irradiated with a pulse from the Nd:Glass laser. Precise alignment with the laser beam's optical axis was achieved with a four-degree-of-freedom positioner. After irradiation, the poly(L-lysine) was taken out of the optical cell and diluted with 0.2-M sodium bromide (NaBr) solution. The dilute solution was in the proportions of 0.5 ml of poly(L-lysine) and 4.5 ml of NaBr solution. The solution was filtered through an 0.8-μm filter and collected in a scattering cell for further studies by means of dynamic light scattering to determine if the IR laser pulse caused a breakdown of the poly(L-lysine) molecules. A control sample was also prepared, which was not exposed to IR laser pulses but was placed in the cell, withdrawn, diluted, and filtered and stored along with the irradiated sample.

Samples of poly(L-lysine) were irradiated by both single ultrashort pulses with energies up to 1.37 mJ/cm^2 and successions of up to four entire pulse trains. Each train consisted of 100 pulses and had integrated energy densities of up to 150 mJ/cm^2 per train.

Calf-Thymus DNA

The experimental protocol for the study of laser-induced damage in calf-thymus DNA was similar to that for poly(L-lysine). Calf-thymus DNA solutions were carefully prepared at a 1-mg/ml concentration in aqueous sodium chloride (NaCl) by dissolving the DNA in the cold room (5°C) for periods of 3-5 days, at a carefully controlled stirring rate of < 1 cycle/sec. Some samples included the Ca++ sequestering agent, EDTA; others did not. In each case both the test and control samples were treated identically except for irradiation by the Nd:Glass laser. Test samples were irradiated by single mode-locked pulses, entire pulse trains, and successions of several pulse trains. To achieve higher energy densities, the small-diameter long cell was used. The test and control samples were then taken out of their respective cells and diluted with 1-M NaCl solution in the ratio of 0.5 ml DNA to 9.5 ml NaCl. The solutions were filtered through either a 3.0- or 1.25-μm filter and collected in scattering cells for the dynamic light scattering experiments.

Purple Membrane

The Statement of Work proposed that it would be most desirable to examine isolated biological macromolecular systems or cells whose electrodynamic properties are similar to retinal tissue. In accordance with this stated purpose and with the concomitant immutability of poly(L-lysine) with respect to radiation damage, we felt it was imperative to look at more promising systems such as the purple membrane patches from the photosynthetic bacterium Halobacterium halobium (HBH).

The purple membrane patches are composed of 75% protein and 25% lipids by weight. The sole protein is bacteriorhodopsin, which is so named because it consists of retinol bound by a Schiff base linkage to an amino group of lysine residue. This is entirely analogous to visual pigment rhodopsin. The two major lipids are phosphatidylglycerophosphate and glycolipidsulfate. Evidence points to these purple membrane patches as a light-induced proton pump. Suspensions of the intact cells show light-induced changes in pH.

Our first step with this material was to find its apparent diffusion constant as a function of scattering angle. Concentrated solutions of HBH were obtained from the laboratory of W. L. Peticolas at the University of Oregon. The stock solution comes in an aggregated form which has to be dispersed into solution. This was done by immersing about 2.5 ml of the concentrated mixture in a 5-ml volumetric flask and then immersing the flask in an ultrasound bath. Visual inspection determined the end point of dispersion. Several drops of the dispersed solution were then diluted in a scattering vessel with filtered (1.2-3 μm) distilled water. Solutions made up this way are stable for months. Future preparations will most likely refine this rough method.

The solution of HBH scatters light extremely well as could be predicted from its characteristic purple color. Thus, one can achieve high signal-to-noise ratios at all angles.

EXPERIMENTAL RESULTS AND DISCUSSION

Poly(L-lysine)

Samples of poly(L-lysine) were irradiated by both single ultrashort pulses with energies up to 1.37 mJ/cm^2 and successions of up to four entire pulse trains, each consisting of ~100 pulses and having integrated energy densities of up to 150 mJ/cm^2. All samples were then studied by the dynamic light scattering method. No detectable difference was found in the photon correlation functions at any angle. All samples that were studied exhibited essentially identical correlation functions at all angles. This forced us to conclude that even a succession of four entire pulse trains of up to 150 mJ/cm^2 each at 1060 nm did not produce any breakage of the poly(L-lysine) molecules. This is probably attributable to the fact that poly(L-lysine) has an extremely small optical anisotropy, as judged from the intensity of depolarized scattered light, so optically induced torques would not be sufficient to break these molecules. (See Appendix: Summary Table.)

Calf-Thymus DNA

To date we have found that single mode-locked pulses 10-15 psec in duration, with an energy density of $\lesssim 0.76$ mJ/cm^2, do not cause any changes in the DNA structure that are detectable by the dynamic light scattering technique.

The results for irradiation by one or several pulse trains (each consisting of ~100 pulses) have indicated damage in some cases, although there is some ambiguity in the data. We have established that irradiation of DNA by one or two successive pulse trains of pure 1060-nm light results in no detectable damage if the energy density in each pulse train is < 120 mJ/cm^2. This result was obtained whether or not EDTA was in the sample. In each case the photon correlation spectrum was determined at several angles--25°, 40°, 90°, 110°--to ensure that any fortuitous agreement between control and test sample occurring at one angle would be detected. No differences were observed at any angle. In one instance a sample did not contain EDTA; however, it was also simultaneously exposed to frequency doubled light (530 nm) having an energy density of 1-1.5 mJ/cm^2 per pulse train. (This resulted from a temporary removal of the dichroic beam splitter, DBA, from the apparatus--see Fig. 7.)

Figures 14 and 15 show the correlation functions for the scattering angles $\theta = 25°$ and $\theta = 90°$, respectively, for this case. (In this case only these two angles were examined.) The correlation functions of the irradiated DNA sample and of the control sample (not irradiated by IR laser pulses) exhibit a marked difference for $\theta = 25°$, as shown in Figure 14. Indeed, when least-squares fitted to single exponentials, the resulting apparent diffusion coefficients,

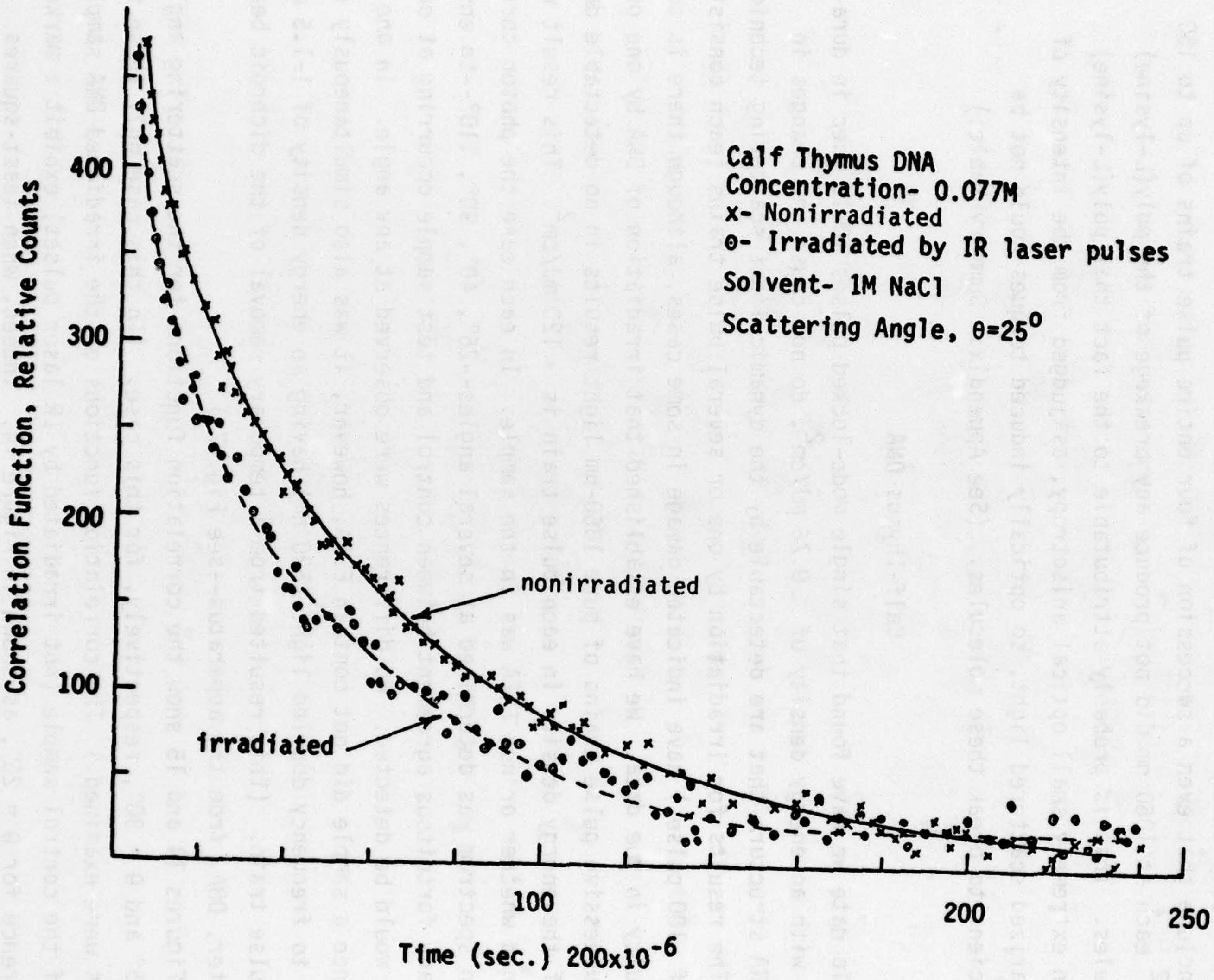

Figure 14. Correlation function of calf-thymus DNA. Scattering angle: 25°.

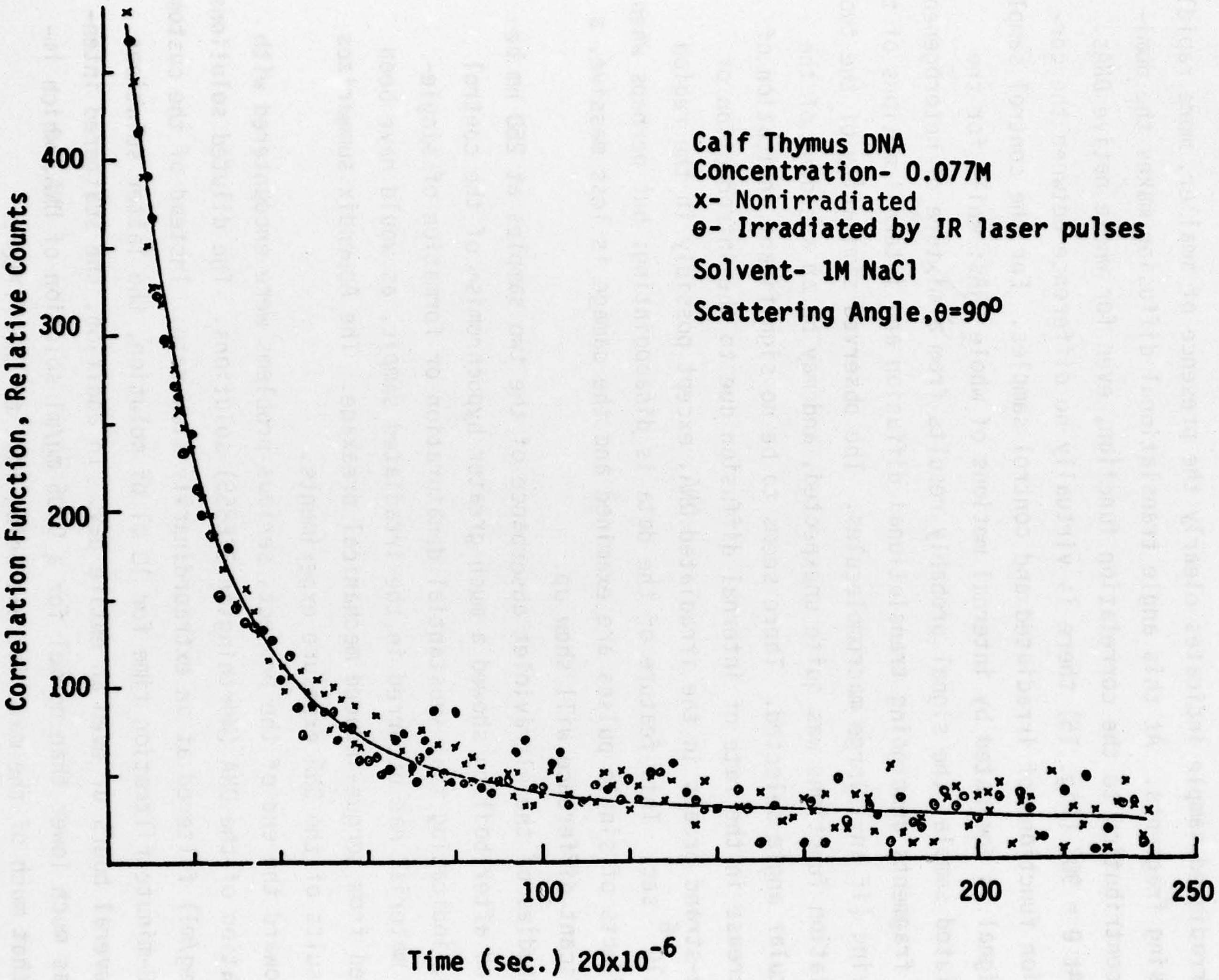

Figure 15. Correlation function of calf-thymus DNA. Scattering angle: 90°.

$D_{irr} = 1.9 \times 10^{-8}$ cm^2/sec and $D_{control} = 1.4 \times 10^{-8}$ cm^2/sec, differed substantially. The very steep initial part of the correlation function for the irradiated sample indicates clearly the presence of smaller, more rapidly diffusing fragments. At this angle translational diffusion makes the dominant contribution to the correlation function, even for whole native DNAs.

At $\theta = 90°$ (Fig. 15) there is virtually no difference between the correlation functions of irradiated and control samples. For the control sample, the signal is dominated by internal motions of whole DNAs; while for the irradiated sample, the signal probably results from a mixture of heterogeneous small fragments undergoing translational diffusion and internal motions of the surviving (if any) large macromolecules. The observed similarity of the two correlation functions was quite unexpected, and may be an accident of the particular angle selected. There seems to be no significant indication of an increase in the rate of internal diffusion due to the introduction of single-strand breaks in the irradiated DNA, except possibly in the region 40-80x10^{-6} sec. This feature of the data is disappointing; but perhaps when the effects of single pulses are examined and the damage is less massive, a significant difference will show up.

Studies of the ultraviolet absorbance of the two samples at 260 nm before and after boiling showed a much greater hypochromism of the control sample, indicating that substantial denaturation or formation of single-strand material had occurred in the irradiated sample, as would have been expected from torque-induced mechanical breakage. The Appendix summarizes the results of the DNA exposure experiments.

Toward the end of the project, serious problems were encountered with preparation of the DNA (Worthington 37E855) solutions. The diluted solutions (0.05 mg/ml) filtered at an extraordinarily slow rate. Instead of the customary 40-minute filtration time for 10 ml of solution, the latter solutions took several hours or even an entire day. In addition, the scattered intensity was much lower than normal for a 0.05 mg/ml solution of DNA, which implied that much of the material was being lost to the filter.

The preparative techniques were thoroughly examined. Over 200 filtrations and light scattering measurements were performed to locate the possible causes. The cleaning, stirring, and diluting stages were all scrutinized for possible introduction of deleterious effects, and new batches and pore sizes of filters were tried. The effects of varying the solution pH were thoroughly investigated; also, new samples of DNA were obtained from the original and other suppliers (Sigma R6C-9630). Of all the parameters examined, two things affected the rate of filtration profoundly. One was the salt concentration. A simple decrease in salt concentration from 1-M to 0.1-M NaCl allowed the filtration rate to recover its normal speed of flow; however, the still-low scattered intensity indicated that problems still existed with too much loss of DNA to the filter (the loss ratio was about 5:1). The second, and more disturbing, factor that affected the rate was the detergent extant in the Millipore filters as a consequence of the manufacturing procedure. After the filters were soaked in a hot solution of EDTA and Na_2CO_3 and then bathed in distilled water, the filtration rate returned to normal speed. Numerous runs with the soaked filters indicate that the problem of slow filtration is almost solved.

Depolarized Scattering Experiment--Depolarized scattering from solutions of DNA was attempted at both finite and zero angle. The purpose was to gather information about rotational and possible internal bending of the macromolecule.

We had anticipated that obtaining correlation functions of the depolarized component of scattered light would be very difficult. Our apprehensions, indeed, were confirmed. The finite-angle depolarized scattering did not yield enough light to perform correlation analysis at the short time delays of interest. The ratio of polarized to depolarized light was about 450:1. The zero-angle depolarized experiment did not work because the cell optics had deteriorated since their original construction. Even when the polarizers and other optics were new, the zero-angle experiment was extremely difficult to perform. The drop in quality of the optical surfaces makes an already difficult task unfeasible.

Purple Membrane Characterization

Two representative correlation functions of purple membrane (HBH), at θ = 25° and θ = 90°, are presented (Figs. 16,17). The apparent diffusion constant

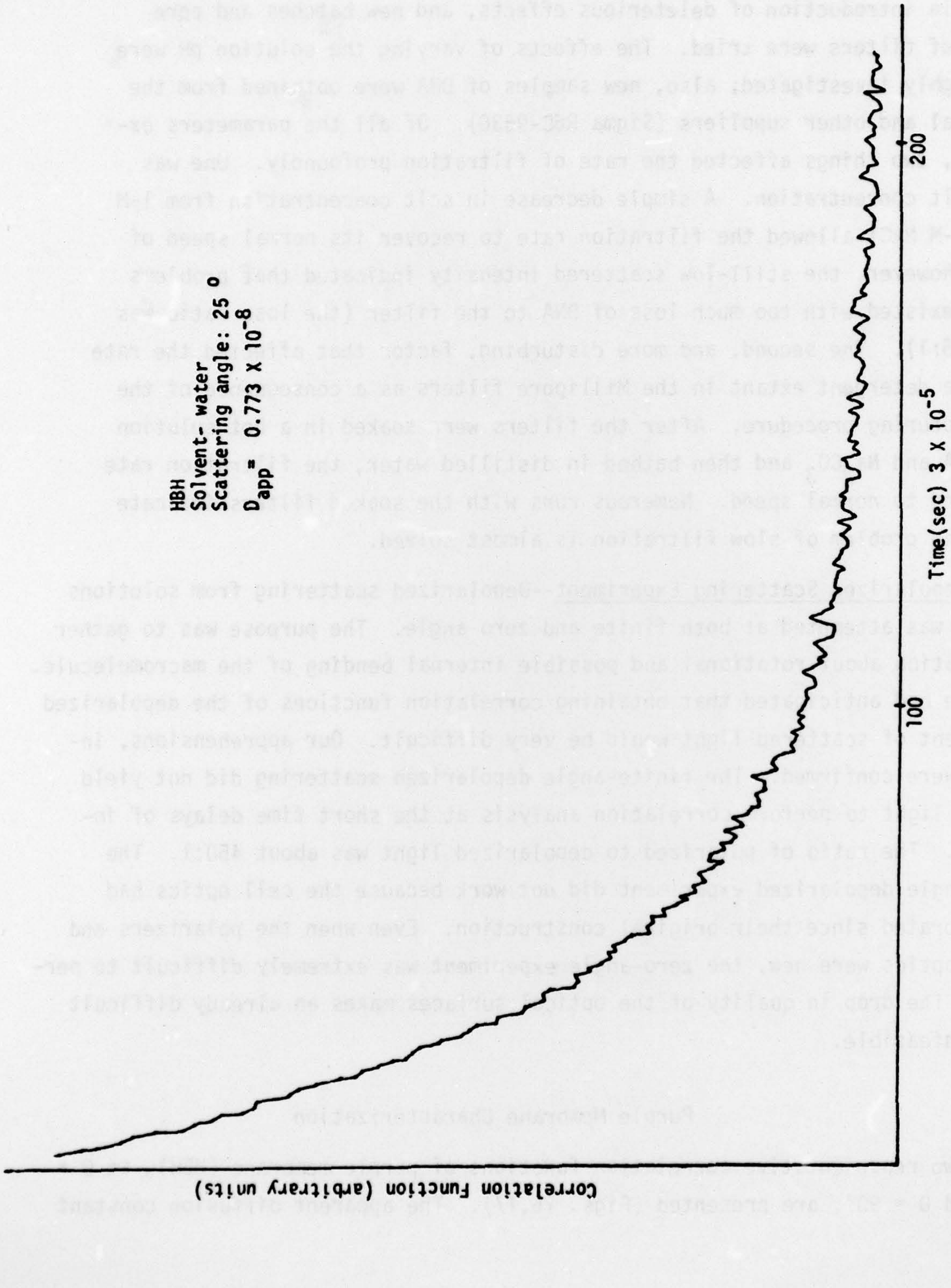

Figure 16. Correlation function of HBH. Scattering angle: 25°.

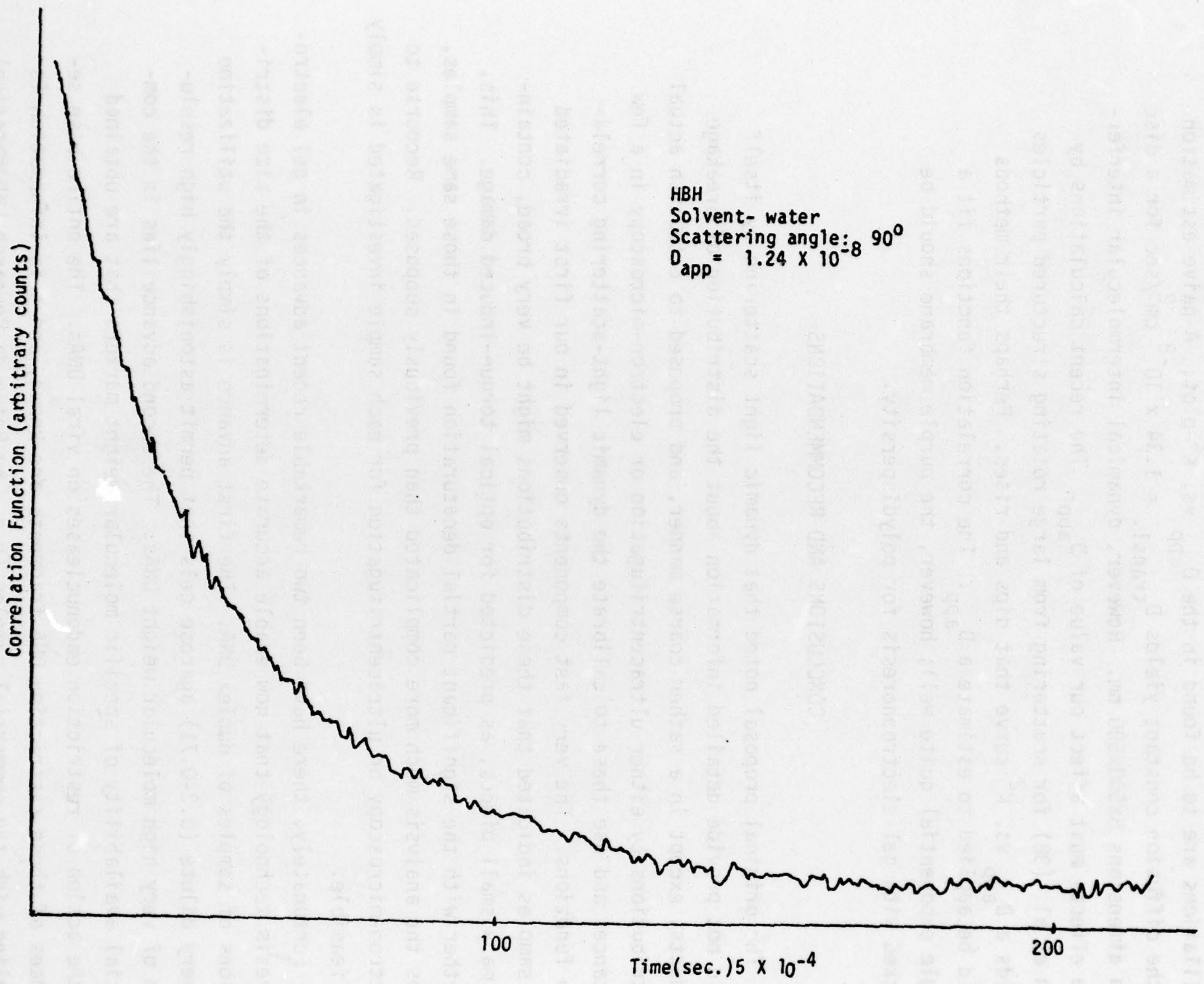

Figure 17. Correlation function of HBH. Scattering angle: 90°.

of HBH varies with θ qualitatively the same way as DNA, except that small oscillations are to be found in the D_{app} vs. K^2 plot. A naive estimation of the diffusion constant yields $D_{transl.} = 1.34 \times 10^{-8}$ cm^2/sec for a disc with dimensions 5x500x500 nm. However, dynamical intermolecular interference effects must affect our value of D_{app}. The recent calculations by Chen et al. (38) for scattering from large rotating structured particles yields a D_{app} vs. K^2 curve that dips and rises. Perhaps their methods could be applied to estimate a D_{app}. The correlation functions fit a single exponential quite well; however, the purple membrane should be checked with gel electrophoresis for polydispersity.

CONCLUSIONS AND RECOMMENDATIONS

The original proposal noted that dynamic light scattering by itself could not provide detailed information about the distribution of breakage products, except in a rather coarse manner, and proposed to establish actual distributions by either ultracentrifugation or electron-microscopy in a few instances and use these to calibrate the dynamic light-scattering correlation functions. The very fast components observed in our first irradiated DNA samples indicated that these distributions might be very broad, containing many small pieces, as predicted for optical torque-induced damage. This, together with the significant partial denaturation found in those same samples, makes the analysis much more complicated than previously supposed. Recourse to electron-microscopy or ultracentrifugation for each sample investigated is simply not feasible.

Fortunately, there have been two remarkable recent advances in gel electrophoresis technology that now enable accurate determinations of the size distributions of samples of duplex DNA. The first advance is simply the utilization of very dilute (0.2-0.7%) agarose gels that permit astonishingly high resolution of very high molecular weight DNAs. The second advance lies in the commercial availability of specific molecular weight markers that are obtained by the action of restriction endonucleases on viral DNAs. The entire base sequences of these restriction DNA fragments are known, and this information is supplied with the commercial samples (e.g., by Bethesda Research Laboratories).

In 0.2% agarose gels the DNA electrophoretic migration distance (in a typical 12-hr run) is proportional to log M (where M is the molecular weight) for molecular weights up to about 2×10^7. The location of the DNA in the gel is determined by applying ethidium bromide, illuminating with UV lights, and observing the resultant visible fluorescence that is emitted only when the dye is complexed to DNA. Simultaneously, parallel electrophoresis of the commercial marker preparations enables the establishment of a precise calibration scale. Although the technique is not rapid, several samples can be run simultaneously on the same gel. Also, the amounts of DNA required are minute, and would enable irradiation studies of much smaller samples (at proportionately higher power levels in the focused beam).

The principal advantage of this technique is that it would permit the complete determination of the breakage product distribution in the irradiated DNA. Such information could prove to be exceedingly valuable in establishing the breakage mechanism. A multimodal distribution of breakage products would imply some specificity in the breakage process, for example.

The use of dynamic light scattering both as an early monitor of damage and as a monitor of subtle forms of damage, including partial denaturation and single-strand breaks, will be necessary and is still in progress. The gel electrophoresis simply offers a convenient and relatively inexpensive way to establish the product distribution for double-stranded fragments. We thus recommend using gel electrophoresis as a "second leg" in the analysis procedure.

We have an almost completed gel electrophoresis apparatus using a J-wick flat-bed configuration designed for very dilute agarose gel (0.5% or less). A specially built safety container for the gel setup is being made. We anticipate that this equipment can be used to analyze for DNA breakage in the future.

REFERENCES

1. Wolbarsht, M. L. (Ed.). Laser applications in medicine and biology. New York: Plenum Press, Vol. 1, 1971, and Vol. 2, 1974.

2. Van Pelt, W. F., et al. A review of selected bioeffects thresholds for various spectral ranges of light. DHEW Publication (FDA) 74-8010, 1973.

3. Sliney, D. H., and B. C. Freasier. Evaluation of optical radiation hazards. Appl Opt 12:1 (1973).

4. Ham, W. T., Jr., et al. Ocular hazard from picosecond pulses of Nd:YAG laser radiation. Science 185:362 (1974).

5. Taboada, J., and R. W. Ebbers. Ocular tissue damage due to ultrashort 1060 nm light pulses from a mode-locked Nd:glass laser. Appl Opt 14:1759 (1975).

6. Zverev, R. M., and V. A. Pashkov. Self-focusing of laser radiations in solid dielectrics. Ah Eksp Teor Fiz 57:1128 (1969); Sov Phys JETP 30:616 (1970).

7. Hellwarth, R. W. In A. J. Glass and A. H. Guenther (eds.). Damage in laser materials, p. 67., U.S. Natl. Bur. Std. Special Publication No. 341, U.S. Dept. of Commerce, Washington, D.C., 1970.

8. Yablonovitch, E. Optical dielectric strength of alkali-halide crystals obtained by laser-induced breakdown. Appl Phys Lett 19:495 (1971).

9. Yablonovitch, E., and N. Bloembergen. Avalanche ionization and the limiting diameter of filaments induced by light pulses in transparent media. Physiol Rev Lett 29:907 (1972).

10. Goldman, L., et al. Studies in laser safety of new high output system: 1 picosecond impacts. Optics Laser Technol 5(1):11 (1973).

11. Chu, B. Laser light scattering. New York: Academic Press, 1974.

12. Schurr, J. M., and K. S. Schmitz. Rotational relaxation of macromolecules determined by dynamic light scattering. I. Tabacco mosaic virus. Biopolymers 12:1021 (1973).

13. Schmitz, K. S., and J. M. Schurr. Rotational relaxation of macromolecules determined by dynamic light scattering. II. Temperature dependence for DNA. Biopolymers 12:1543 (1973).

14. Lee, W. I., and J. M. Schurr. Dynamic light scattering studies of poly-L-lysine HBr in the presence of added salt. Biopolymers 13:903 (1974).

15. Schurr, J. M. Dynamic light scattering of biopolymers and biocolloide. CRC Crit Rev Biochem 4:371 (1977).

16. Schurr, J. M. Relaxation of rotational and internal modes of macromolecules determined by dynamic scattering. Quart Rev Biophys 9:109 (1976).

17. Rouse, P. E., Jr. A theory of the linear viscoelastic properties of dilute solutions of coiling polymers. J Chem Phys 21:1272 (1953).

18. Zimm, B. H. Dynamics of polymer molecules in dilute solution: Viscoelasticity, flow birefringence and dielectric loss. J Chem Phys 24:269 (1956).

19. Callis, P. R., and N. Davidson. Flow dichroism of DNA: A new apparatus and further studies. Biopolymers 7:335 (1969).

20. Callis, P. R., and N. Davidson. Hydrodynamic relaxation times of DNA from decay of flow dichroism measurements. Biopolymers 8:379 (1969).

21. Schurr, J. M. Relaxation times manifested by the Rouse-Zimm model in dynamic light scattering experiments. Biopolymers (in press).

22. Wilkinson, R. S., and G. B. Thurston. The optical birefringence of DNA solutions induced by oscillatory electric and hydrodynamic field. Biopolymers 15:1555 (1976).

23. Ferry, J. D. Viscoelastic properties of polymers. New York: Wiley, 1961.

24. de Gennes, P.-G. Quasi-elastic light scattering of neutrons by dilute polymer solutions: I. Free-draining limit. Physics 3:37 (1967).

25. du Bois-Violett, E., and P.-G. de Gennes. Quasi-elastic light scattering by dilute ideal polymer solutions: II. Effects of hydrodynamic interactions. Physics 3:181 (1967).

26. Silbey, R., and J. M. Deutch. Quasi-elastic light scattering from large macromolecules. J Chem Phys 57:5010 (1972).

27. Lee, W. I., and J. M. Schurr. Intensity autocorrelation function for a flexible polymer. Chem Phys Letts 23:603 (1973).

28. Lin, S.-C., and J. M. Schurr. Dynamic light scattering studies of internal motions in DNA. I. Applicability of the Rouse-Zimm model. Biopolymers 17:425 (1978).

29. Bloembergen, N., and E. Yablonovitch. Infrared-laser-induced unimolecular reactions. Phys Today 31:23 (1978).

30. Bloomfield, V. A., et al. Physical chemistry of nucleic acids. New York: Harper and Row, 1974.

31. Bruckner, A. P. Some applications of picosecond optical range-gating. Proc SPIE 94:41 (1976).

32. Bruckner, A. P. Picosecond light scattering measurements of cataract microstructure. Appl Opt (in press).

33. DeMaria, A. J. Picosecond laser pulses. Proc IEEE 57:2 (1967).

34. Duguay, M. A., and J. W. Hansen. An ultrafast light gate. Appl Phys Lett 15:192 (1969).

35. Fischer, R., and R. Rossmanith. A Kerr camera with ten picosecond time resolution. Opt Commun 5:53 (1972).

36. Bradley, D. J., and G. H. C. New. Ultrashort pulse measurements. Proc IEEE 62:313 (1974).

37. Chen, S. H., et al. Simple digital clipped correlator for photon correlation spectroscopy. Rev Sci Instrum 46:1356 (1975).

38. Chen, S. H., et al. Quasi-elastic light scattering from structured particles. Appl Opt 16:187 (1977).

APPENDIX

SUMMARY TABLE

Poly(L-lysine)

Number of pulses	Energy density (mJ/cm^2)	Energy/pulse (mJ/cm^2)	Breakage results
1	1.4	1.4	negative
2	2.8	1.4	negative
4 pulse trains (100 pulses/train)	600	∿1.5	negative

Calf-Thymus DNA

Number of pulses	Energy density (mJ/cm^2)	Energy/pulse (mJ/cm^2) (mean)	EDTA	Breakage results; comments
Short cell:				
1	0.76	0.76	yes	negative
1	<0.5	<0.5	no	negative
1	0.5	0.5	no	negative
2	1.5	0.75	yes	negative
1 train	58.5	0.59	yes	negative
1 train	59.0	0.56	yes	negative
1 train	116	1.1	yes	negative
2 trains	110	0.55	yes	negative; slow filtration; low scattering intensity
2 trains	230	1.15	yes	negative
4 trains	500 (±20%)	∿1.2	no	positive
5 trains	440	0.88	yes	negative
4 trains (530 nm)	6.8 (±50%)	$\sim 1.7 \times 10^{-2}$	yes	ambiguous
Long cell:				
1 train	556	5.6	yes	ambiguous; slow filtration; low scattering intensity
1 train	800	8	yes	ambiguous; slow filtration; low scattering intensity

In all cases except the last two, the results were negative at irradiation energy densities lower than those indicated. Probable error in energy measurements is ± 5% except where noted.